Title
Impacts of elevated dissolved CO2 on a shallow groundwater system: Reactive transport modeling of a controlled-release field test

Authors

Zheng, Liange
Spycher, Nicolas
Bianchi, Marco
et al.

Publication Date

2016-12-01

DOI
10.1016/j.chemgeo.2016.10.027

Impacts of elevated dissolved CO_2 on a shallow groundwater system: Reactive transport modeling of a controlled-release field test

Author links open overlay panelLiangeZheng[a]NicolasSpycher[a]MarcoBianchi[b]John D.Pugh[c]CharulekaVaradharajan[a]Ruth M.Tinnacher[a]Jens T.Birkholzer[a]PeterNico[a]Robert C.Trautz[d]
Show more

https://doi.org/10.1016/j.chemgeo.2016.10.027Get rights and content

Abstract

One of the risks that CO_2 geological sequestration imposes on the environment is the impact of potential CO_2/brine leakage on shallow groundwater. The reliability of reactive transport models predicting the response of groundwater to CO_2 leakage depends on a thorough understanding of the relevant chemical processesand key parameters affecting dissolved CO_2 transport and reaction. Such understanding can be provided by targeted field tests integrated with reactive transport modeling. A controlled-release field experiment was conducted in Mississippi to study the CO_2-induced geochemical changes in a shallow sandy aquifer at about 50 m depth. The field test involved a dipole system in which the groundwater was pumped from one well, saturated with CO_2 at the pressure corresponding to the hydraulic pressure of the aquifer, and then re-injected into the same aquifer using a second well. Groundwater samples were collected for chemical analyses from four monitoring wells before, during and after the dissolved $CO_2$was injected. In this paper, we present reactive transport models used to interpret the observed changes in metal concentrations in these groundwater samples. A reasonable agreement between simulated and measured concentrations indicates that the chemical response in the aquifer can be interpreted using a conceptual model that encompasses two main features: (a) a fast-reacting but limited pool of reactive minerals that responds quickly to changes in pH and causes a pulse-like concentration change, and (b) a slow-reacting but essentially unlimited mineral pool that yields rising metal concentrations upon decreased groundwater velocities after pumping and injection stopped. During the injection, calcite dissolution and Ca-driven cation exchange reactions contribute to a sharp pulse in concentrations of Ca, Ba, Mg, Mn, K, Li, Na and Sr, whereas desorption reactions control a similar increase in Fe concentrations. After the injection and pumping stops and the groundwater flow rate decreases, the dissolution of relatively slow reacting minerals such as plagioclase drives the rising concentrations of alkali and alkaline earth metals observed at later stages of the test, whereas the dissolution of amorphous iron sulfide causes slowly increasing Fe concentrations.

Graphical abstract

A controlled-release field experiment was conducted in Mississippi to study the CO_2-induced geochemical changes in a shallow sandy aquifer at about 50 m depth. The field test involved a dipole system in which the groundwater was pumped from one well, saturated with CO_2 at the pressure corresponding to the hydraulic pressure of the aquifer, and then re-injected into the same aquifer using a second well. A reasonable agreement between simulated and measured concentrations indicates that the chemical response in the aquifer can be interpreted using a conceptual model that encompasses two main features: (a) a fast-reacting but limited pool of reactive minerals that responds quickly to changes in pH and causes a pulse-like concentration change, and (b) a slow-reacting but essentially unlimited mineral pool that yields rising metal concentrations upon decreased groundwater velocities after pumping and injection stopped. During the injection, calcite dissolution and Ca-driven cation exchange reactions contribute to a sharp pulse in concentrations of Ca, Ba, Mg, Mn, K, Li, Na and Sr, whereas desorption reactions control a similar increase in Fe concentrations.

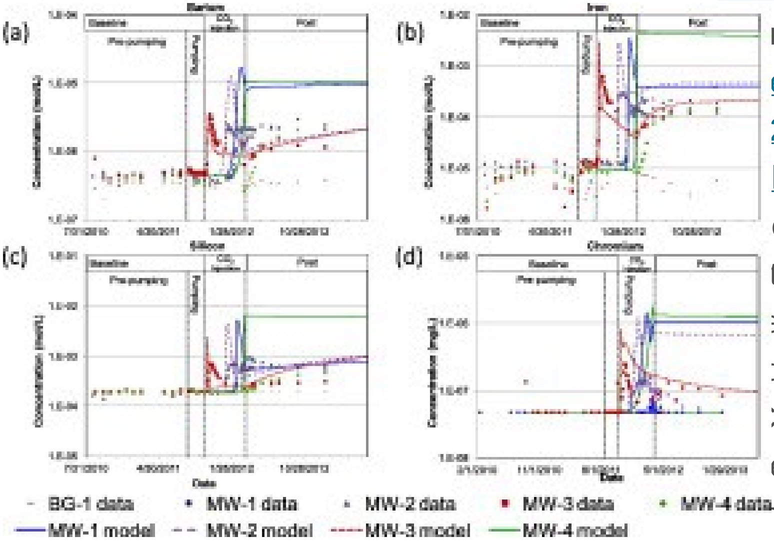

1. Download high-res image (245KB)
2. Download full-size image

- **Previous** article
- **Next** article

1. Introduction

Ever since the concept of CO_2 geologic storage was proposed about two decades ago, many studies have been undertaken to assess hydrological, geochemical and mechanical processes affecting deep injection and containment of CO_2 in storage reservoirs. Meanwhile, as part of environmental risk assessmentsfor CO_2 storage sites, studies have also been undertaken to assess the impacts of potential CO_2 leaks from deep storage reservoirs, on the quality of overlying fresh water aquifers (see review papers by Lemieux, 2011 and Harvey et al., 2012, and references therein). Numerical modeling has been an important tool to address this issue.

Reactive transport models were first used to evaluate the potential impacts of CO_2 leakage on the water quality of shallow, overlying aquifers (Wang and Jaffe, 2004, Carroll et al., 2009, Zheng et al., 2009, Apps et al., 2010, Wilkin and Digiulio, 2010), and to identify potential issues such as the leaching out of organics such as BETX, PAH, from source rocks (Zheng et al., 2013, Zhong et al., 2014). Later on, they were used to rpret data from laboratory eriments (e.g. Viswanathan et al., 2012, Zheng et 2016) and field tests (e.g. Zheng et al., 2012, Trautz l., 2013 and Zheng et al., 2015) in order to erstand key physical and chemical processes that trol the response of aquifers to CO_2leakage. Most ently, reactive transport models have been used to dict potential long-term change in aquifer in response O_2/brine leakage (Bacon et al., 2016), to conduct ertainty quantifications (Hou et al., 2014) to lay the ndation for risk assessment studies, and to provide guidance for risk management and mitigation.

Laboratory experiments provide useful information on the type and quantity of trace elements that may be mobilized in response to CO_2 intrusion into potable groundwater, forming the basis for further modeling analyses. Such experiments (Smyth et al., 2009, Lu et al., 2010, Little and Jackson, 2010, Wei et al., 2011, Viswanathan et al., 2012, Humez et al., 2013Varadharajan et al., 2013, Wunsch et al., 2014, Kirsch et al., 2014, Lawter et al., 2016) were typically conducted in batch or column mode, where CO_2 was released into a pre-equilibrated water-rock environment and the geochemical changes in the aqueous phases were monitored subsequently. Modest to strong increases in concentrations of major and trace elements have typically been reported in these laboratory experiments, although in terms of the changes of one particular element, different experiments have led to different results. For example, increases in Fe concentration has been reported in Smyth et al. (2009) and Lu et al. (2010), whereas Humez et al.

(2013) observed declining Fe concentrations after initial CO_2 influx. The increase or decrease in metal concentrations also varies significantly from one experiment to another, likely due to differences in experimental conditions, types of sediments, mineralogical compositions, etc. However, despite these differences, one common observation is a concentration increase for alkali and alkaline earth metals and Si.

Laboratory experiments have some inherent limitations such as (1) failing to preserve the in situ water-rock environment as a result of pre-equilibration of sediments with a synthetic solution (e.g., Smyth et al., 2009) or DI water (Lu et al., 2010), (2) unwanted oxidation of sediments samples during the experiment (e.g., Little and Jackson, 2010), or (3) the failure to include transport of groundwater and CO_2.

Several field tests have been conducted to further enhance our understanding of potential impacts of CO_2 leakage on shallow groundwater. The ZERT (Zero Emissions Research and Technology) field test in Montana, USA (Kharaka et al., 2010, Spangler et al., 2010) was probably the first controlled-release experiment in this regard, with food-grade CO_2 injected over a 30 day period into a horizontal perforated pipe a few feet below the water table of a shallow aquifer. Cahill and Jakobsen (2013) and Cahill et al. (2014) reported a field scale pilot test in which CO_2 gas was injected at 5–10 m depth into an unconfined aquifer in Denmark for two days, and water geochemistry changes were monitored for more than 100 days. As reported in Peter et al. (2012), CO_2 was injected through 3 wells for a period of 10 days into an aquifer at 18 m depth in Northeast Germany. All these tests involved an injection of CO_2 or CO_2-bearing water into the aquifer, and the monitoring of changes in water composition via monitoring wells downstream of the injection point. In general, observations made in field tests are largely consistent with those from laboratory tests in terms of concentration increases for major and trace elements, but there are two noticeable differences: first, the level of concentration changes observed in the field is typically much lower than in the laboratory. For example, an increase in major and trace element concentrations of 1 to 3 orders of magnitude has been observed in the laboratory compared to field tests, which never show an increase greater than one order of magnitude (i.e., 20% to 700%). Secondly, concentration increases in trace elements, especially for elements of environmental concern such as As, Pb, Ba, Cd, are more frequently observed in laboratory than in field tests.

A thorough understanding of key physical and chemical processes and related parameters is critical for building a reliable model to predict long term changes in aquifer response to CO_2/brine leakage. Researchers have postulated based on laboratory-scale experimental results (e.g. Lu et al., 2010), the simulation of laboratory-scale data (e.g. Humez et al., 2011, Viswanathan et al., 2012, Zheng et al., 2015b) or field tests (e.g. Zheng et al., 2012, Trautz et al., 2013) that a number of chemical processes are potentially responsible for the mobilization of trace elements. These include the dissolution of carbonates (e.g., Kharaka et al., 2006, McGrath et al., 2007, Lu et al., 2010), sulfides (e.g., Wang and Jaffe, 2004, Zheng et al., 2009, Apps et al., 2010) and iron oxyhydroxide minerals (e.g., Kharaka et al., 2006, Kharaka et al., 2009), as well as surface reactions such as adsorption/desorption (Viswanathan et al., 2012) and ion exchange (Kharaka et al., 2006, Kharaka et al., 2009, Zheng et al., 2009, Apps et al., 2010, Zheng et al., 2012, Cahill et al., 2014). The degree to which these reactions contribute to water quality impacts depends on the specific aqueous chemistry and aquifer mineralogy for a given system. Field testing integrated with reactive transport modeling provides an effective and reliable way to identify reactions and parameters that are needed to build reliable simulation tools for risk assessments of CO_2 sequestration.

A comprehensive longer-term field study involving the controlled release of groundwater containing dissolved CO_2 was initiated in 2011 to investigate potential groundwater impacts in Mississippi, USA (Trautz et al., 2013). Injection of dissolved CO_2 lasted approximately 5 months followed by an extended phase of post-injection groundwater monitoring. The experiment involved extensive laboratory and field characterization of groundwater and sediments, an innovative fluid-delivery system, hydrologic monitoring, and geophysical monitoring for remote detection of dissolved CO_2. Trautz et al. (2013) presented the data from this test at one of the monitoring wells, including preliminary results of reactive transport simulations, and Varadharajan et al. (2013)reported laboratory test results for aquifer sediments collected while drilling wells for this test. In this paper, we present reactive transport simulations conducted to interpret groundwater monitoring data at the site over a significantly longer time frame than initially reported by Trautz et al. (2013), with the goal to elucidate key chemical processes and parameters that could affect observed changes in long-term dissolved metal concentrations in groundwater at this test site.

2. Field test

2.1. Test description

The study site is located in Jackson County Mississippi and lies in the Pascagoula River Drainage Basin in the Gulf Coastal Plainphysiographic province, which is topographically gently rolling to flat with local salt marshes. The stratigraphic interval into which carbonated water was injected is composed of fine silty sand with minor clay interbedding at depths between 46.9 and 54.6 m (Fig. 1, right). An innovative closed loop groundwater delivery system was used to pump groundwater from the confined shallow aquiferthrough a carbonation unit to infuse it with CO_2 before injecting the carbonated groundwater back into the same shallow aquifer. The test configuration is shown in Fig. 1: groundwater is injected through well IW-1 and pumped out from well PW-1. Groundwater samples were collected from the five monitoring wells over three test periods (Table 1): (1) for 13 months prior to pumping and injection (background), (2) for five months during pumping and injection, and (3) for 10 months after pumping and injection ended. Groundwater samples were analyzed in the laboratory to evaluate trends in major and minor cations, anions, trace elements, organic carbon, and dissolved gases. In addition, geophysical monitoring using complex electrical tomography allowed changes in electrical resistivity of the groundwater to be observed, and the position of the dissolved CO_2 plume as it migrated between wells to be tracked (Dafflon et al., 2013).

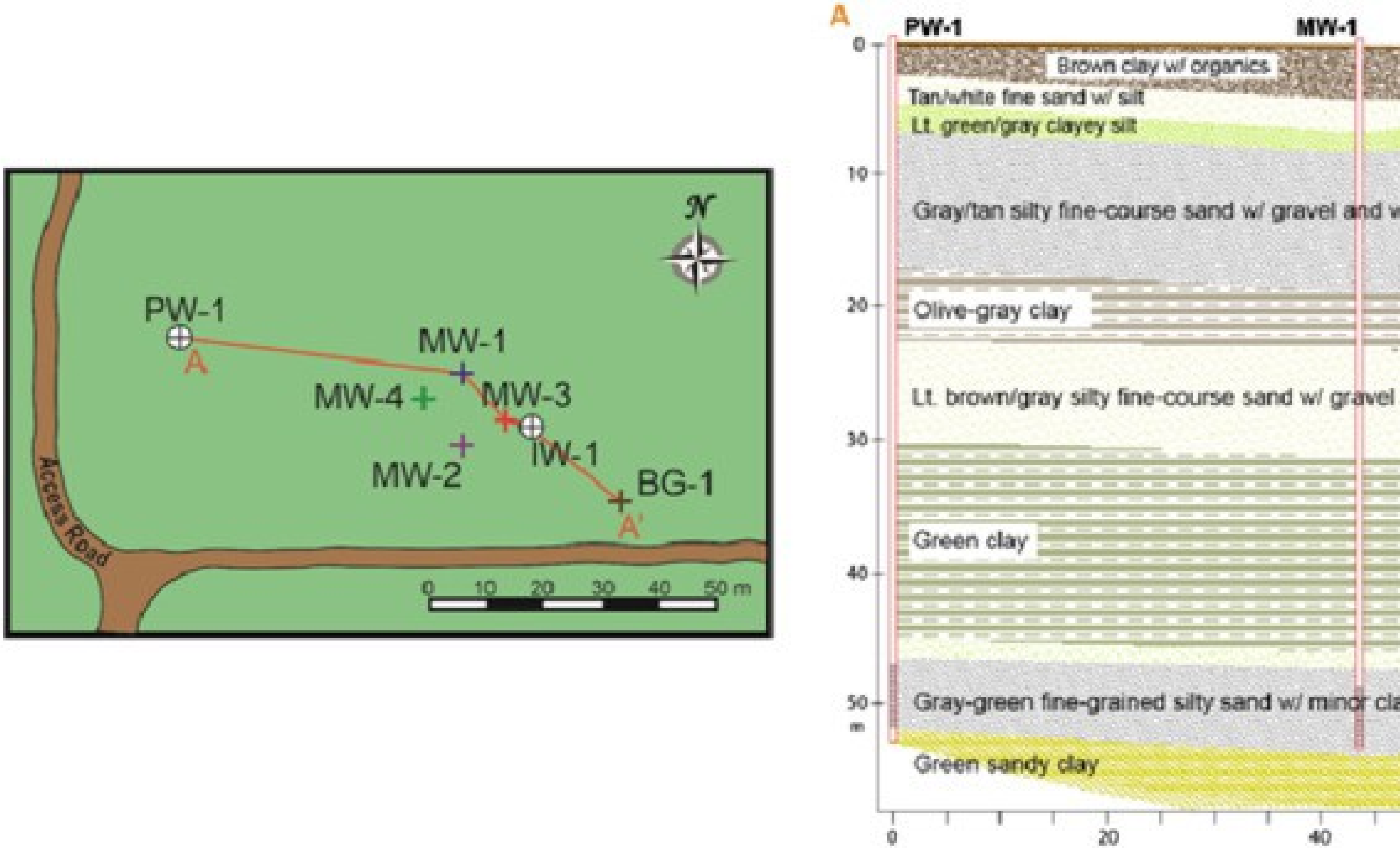

1. Download high-res image (325KB)
2. Download full-size image

Fig. 1. Schematic showing plan view of the well field (left) and geologic cross-section A–A′ (right). Well abbreviations refer to the pumping well (PW), the injection well (IW), the monitoring wells (MW) and the background well (BG) used to characterize the pristine groundwater composition not affected by CO_2 injection.

Table 1. Test period durations.

Test period	Start date	End date	Approx. duration (months)
Pre-CO_2 injection baseline	2-Sep.-2010	18-Oct.-2011	13
Pre-pumping (static baseline)	2-Sep.-2010	12-Aug.-2011	11
Pumping (dynamic baseline)	12-Aug.-2011	18-Oct.-2011	2
CO_2 injection (pumping continues)	18-Oct.-2011	23-Mar.-2012	5
Post-CO_2 injection	23-Mar.-2012	15-Jan.-2013	10

A decrease in groundwater pH by 1.5–2 units was

Environmental Protection Agency under the Clean Water Act.

2.2. Trend analyses of observed metal concentrations

In previous work, we reported on the early-time groundwater composition trends observed during the first few months after injection of carbonated water started (Trautz et al., 2013). For several metals (Ba, Ca, Fe, Li, Mg, Mn, K, Si, Na, Sr), the concentration data exhibited a clear “pulse”-like response (see Fig. 2 for Sr as example) upon arrival of carbonated groundwater at the monitoring well closest to the injection point (MW-3). This response was attributed to Ca-driven exchange reactions triggered by the dissolution of a very small, finite amount of calcite in the sediments.

As groundwater quality data continued to be collected over a longer time frame, it became evident that the concentration of some metals (e.g., Ca, Ba, Fe) started to slowly increase once pumping and injection ended and the groundwater velocities returned to ambient conditions (Zheng et al., 2015). This later increase (superposed on an initial fast, exchange-driven pulse) was attributed to slow mineral dissolution, noticeable only under conditions of increased groundwater residence time once the pump was turned off (Zheng et al., 2015).

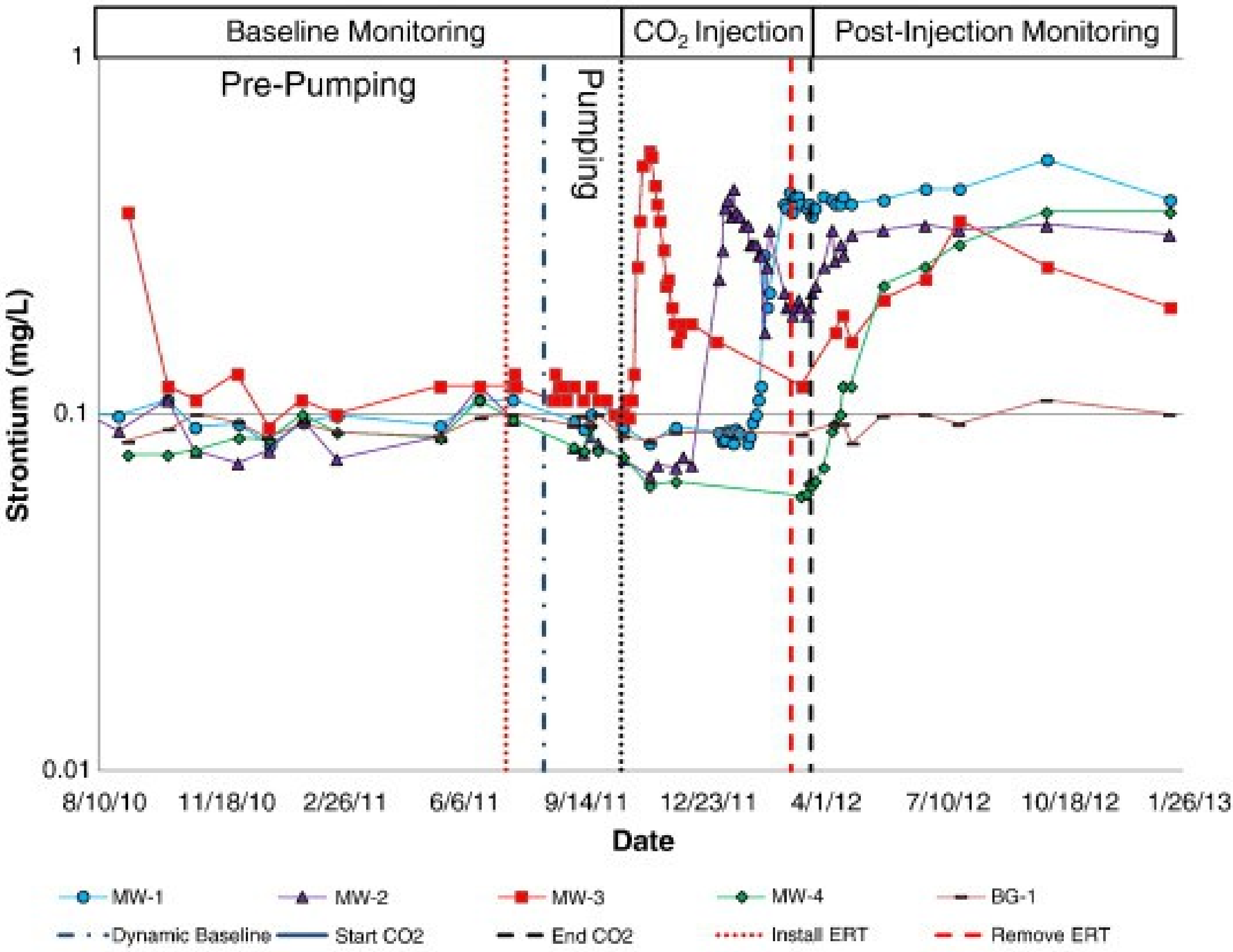

1. Download high-res image (459KB)
2. Download full-size image

Fig. 2. Strontium concentrations in groundwater illustrating the trend of Type III metals mobilized by the carbonation of groundwater, with highest peak concentrations observed at MW-3. Trends of pH changes are shown in Fig. 6 for all monitoring wells.

Here, we further evaluate the groundwater quality response to carbonation using the *full* set of analytical data collected *before*(13 months), *during* (5 months), and *after* the release of CO_2(10 months after turning off the injection pump). Accordingly, the monitoring data were classified into three groups: *pre*-, *during*, and *post*-injection, with the '*pre*-injection' data defined as analyses before the arrival of the carbonated plume at specific wells, measured as the

e

npled

.

,

)

n

ι

arrow

s

etals

ons

d

ered

ich

ease

y)

also

show some correlation of Ca with Fe, Na, and alkalinity, as well as a good correlation between Fe and Mn. A weaker correlation of Si with Ca (Fig. 3) (and also Na, not shown) although quite more scattered, also lends support to the hypothesis of Zheng et al. (2015) suggesting that the slow dissolution of plagioclase may contribute to the long-term concentration trends of these elements.

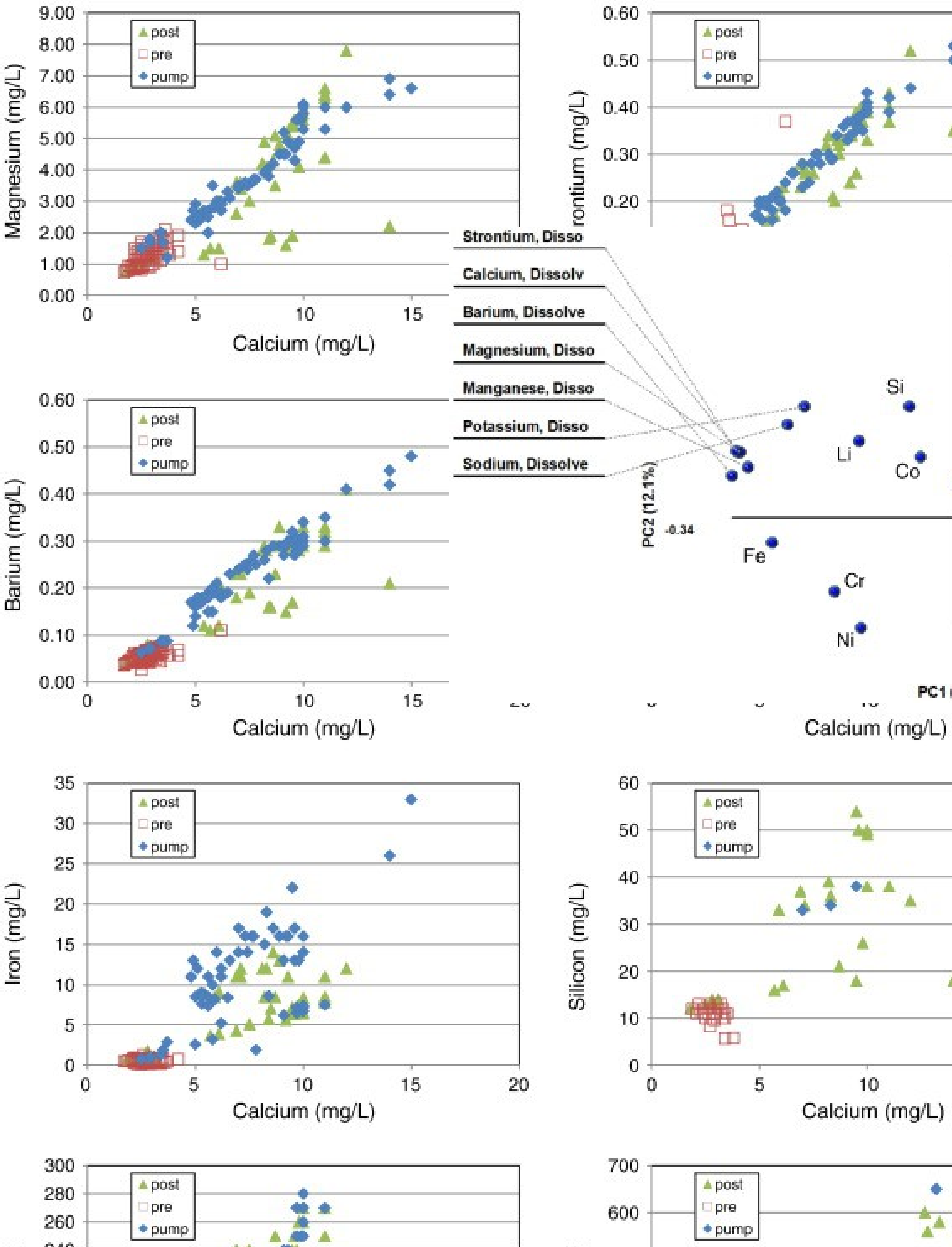
Magnesium (mg/L)
9.00
8.00
7.00
6.00
5.00
4.00
3.00
2.00
1.00
0.00
Calcium (mg/L)
0
5
10
15
post
pre
pump
rontium (mg/L)
0.60
0.50
0.40
0.30
0.20
Strontium, Disso
Calcium, Dissolv
Barium, Dissolve
Magnesium, Disso
Manganese, Disso
Potassium, Disso
Sodium, Dissolve
Si
Li
Co
Fe
Cr
Ni
PC2 (12.1%)
-0.34
PC1
Barium (mg/L)
0.60
0.50
0.40
0.30
0.20
0.10
0.00
Iron (mg/L)
35
30
25
20
15
10
5
0
20
Silicon (mg/L)
60
50
40
30
20
10
0
300
280
260
700
600

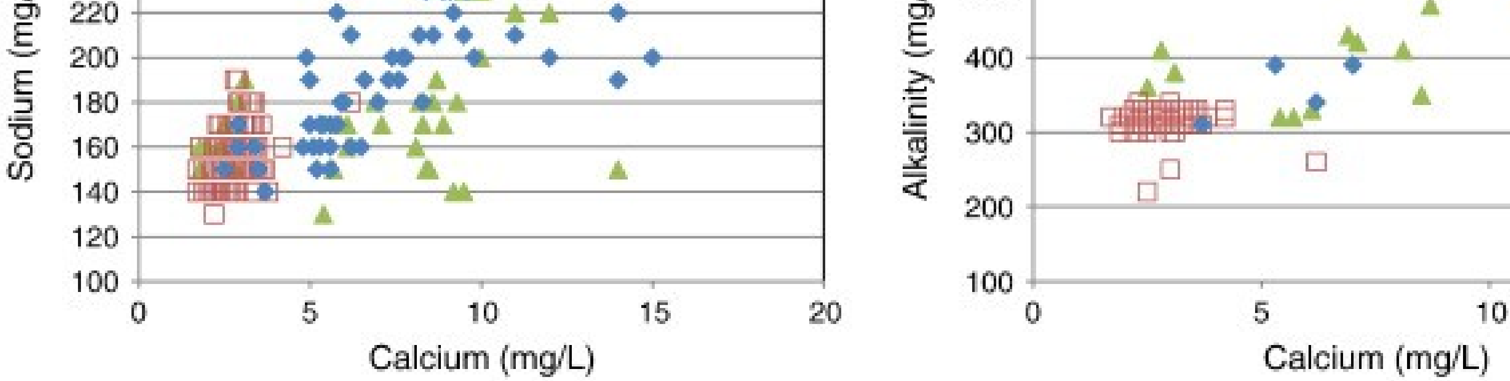

group of released metals. Second, Fe, Cr, and Ni appear to form their own group (lower left quadrant in Fig. 4), suggesting another source and/or release mechanism for these elements in the field study. No release was observed for these metals in leaching experiments (Varadharajan et al., 2013). One possible explanation is a contamination of groundwater samples with corrosion products from stainless steel geophysical electrodes that were deployed in the field but not present in lab-scale experiments. Third, alkalinity, chloride, and dissolved organic matter also fall within the top 10 contributors, but in this case because of their individual variability, or lack thereof.

2.3. Postulated metal release mechanisms

The release of trace elements from sediments due to reaction with dissolved CO_2 has been explained by various mechanisms including: (1) the dissolution of calcite with trace amounts of impurities of other elements (Lu et al., 2010), (2) metal desorptionfrom mineral surfaces (Viswanathan et al., 2012, Zheng et al., 2012), (3) the dissolution of silicate minerals (Yang et al., 2013), and/or (4) cation exchange reactions, which are triggered by an increase in Ca^{+2} concentrations after calcite dissolution (Zheng et al., 2012). To date, metal concentration trends observed in most tests reported in the literature have been monotonic increases, mainly because laboratory tests were typically performed in batch experiments—without any transport component—and most field tests were conducted over fairly short time periods (Kharaka et al., 2010). One first upon arrival of the carbonated groundwater, but then decreased during the remaining CO_2injection period, and continued to decrease over the post injection time-period. In contrast, during the field test conducted for the present study, a rapid pulse-like release of dissolved cations upon the arrival of carbonated groundwater was observed, followed by slowly-rising cation concentrations almost immediately after the injection was stopped.

This latter behavior can be explained by a conceptual model that includes two contaminant release source terms (Zheng et al., 2015): (a) a fast-reacting but limited pool of reactive minerals that responds quickly to changes in pH, and (b) a slow-reacting but essentially unlimited mineral pool that yields slowly rising concentrations upon decreased groundwater velocities (increased residence time) after pumping and injection stopped. The fast-reacting and slow-reacting pools, and the associated release processes, are believed to differ for different elements, as summarized in Table 2 and discussed in further detail below. The geochemical models developed in this study were set up to simulate the minerals (pools) and processes postulated in this table.

Table 2. Fast-reacting, limited and slow-reacting, unlimited pools proposed for the release of Type III metals.

Element	Fast-reacting limited pool	Slow-reacting unlimited po
Ca	Calcite dissolution	Plagioclase (Ab80An20) dissolution
Ba, Mg, Mn, K, Li, Na, Sr	Cation exchange with Ca	No specific minerals. However, Ca fro reacting Ca pool (plagioclase) triggers cation exchange with these metals.
Fe	Desorption	Iron sulfide (FeS_m) dissolution
Si	Desorption	Plagioclase (Ab80An20) dissolution

3. Groundwater flow and geochemical model development

The reactive transport models in this paper focus on the Type (III) metals/metalloids discussed earlier, because the increasing dissolved concentration of these metals upon exposure to CO_2-saturated water is obviously of more potential concern than the decreasing or un-detectable concentrations of the other metals. The simulations were conducted with TOUGHREACT V2 (Xu et al., 2011), a numerical model that was developed by introducing reactive chemistry into the existing framework of a non-isothermal multi-phase multi-component fluid and heat flow simulator, TOUGH (Pruess et al., 1999).

3.1. Model domain and discretization

Because the aquifer was found to be fairly homogeneous in the vertical direction, a 2-D planar (X-Y) model was employed. The spatial domain of the groundwater flow covers an area of about 500 m × 500 m. An area of 40 m × 100 m was finely discretized with a 1-m grid size. Areas of 20 m × 40 m surrounding the injection well and monitoring wells have even finer gridding with a 0.5-m grid size (Fig. 5). A honeycomb mesh structure was used to minimize numerical errors resulting from the radial groundwater flow pattern around injection and monitoring wells, and other cases of flow vector orientations deviating significantly from a direction perpendicular to interfaces between model grid blocks.

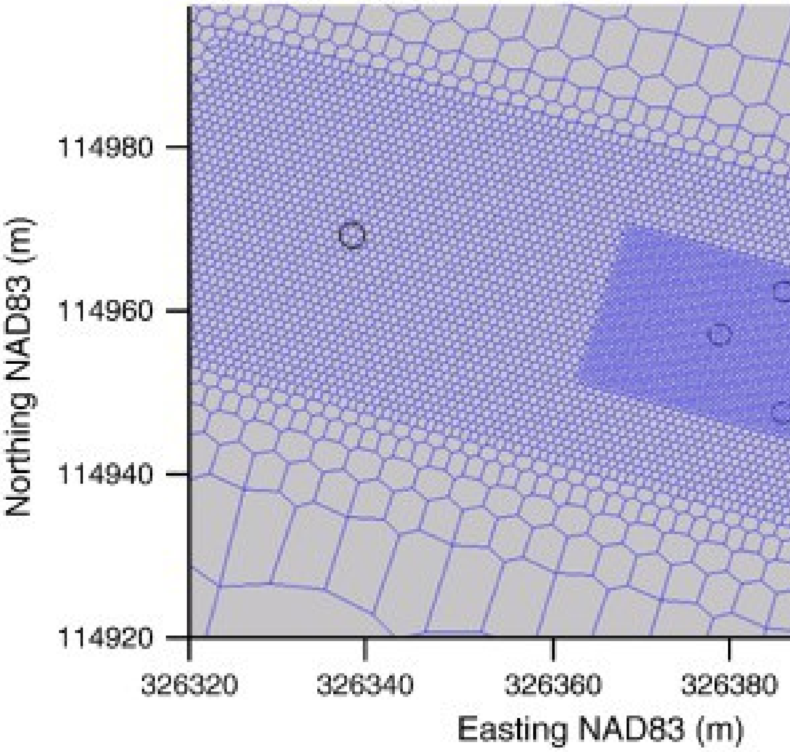

Fig. 5. Close-up view of the model discretization in the area of interest. The centers of the circles correspond to the positions of wells.

3.2. Hydrological parameters

Hydrodynamic parameters used in the model are listed in Table 3. Two pumping tests were conducted to measure the hydraulic conductivity. Drawdown data from a 39-h pumping test were used to calculate an average hydraulic conductivity of 41 ft./day (12.5 m/day or 1.45×10^{-4} m/s) and a storativity of 0.00017 for the transmissive stratigraphic interval in which the test was conducted. Data from another 18-h pumping test yielded close agreement with a hydraulic conductivity of 47 ft./day (14.3 m/day or 1.65×10^{-4} m/s) and a storativity of 0.00029. The hydraulic conductivity used in the model is the average of values from these two pumping tests (13.4 m/day), corresponding to a permeability of 1.55×10^{-11} m^2. The storativity used in the model was taken as 0.00023, which was converted to a pore compressibility of 3.8×10^{-9} Pa^{-1} assuming zero water expansivity.

Table 3. Hydrodynamic parameters used in the model.

Parameter
Porosity ϕ
Permeability [m^2]
Hydraulic conductivity (m/day)
Pore compressibility (Pa^{-1})
Average molecular diffusion coefficient (m^2/s) for all aqueous species
Dispersivity
Tortuosity

[a] Based on the Millington and Quirk (1961) equation.

In TOUGHREACT, hydrodynamic dispersion is not computed. The effect of dispersion is approximated by numerical dispersion, which is roughly equal to half the spacing of grid blocks and in the present case corresponds to dispersivity values between 0.25 m close to the injection well and 0.5 m further away.

3.3. Geochemical parameters

Table 4 lists the chemical composition of initial (ambient) pore water and injected water in the model. The initial composition of the modeled water was based on average concentrations measured over a 20-month pre-injection baseline period. Detection limits were used for the concentration of species for which concentrations were below the detection limit. The pH and carbonate composition of the injected water were computed by assuming equilibration of the initial water with a partial CO_2pressure (P_{CO2}) of 3.8 bar, corresponding to full saturation of the water with CO_2 gas at the prevailing local hydrostatic pressure. The pH value obtained in this manner (4.97) is consistent with measured pH values in the field (~ 5) after injection started. The injected water has essentially the same composition as the initial water except for its lower pH and higher total dissolved carbonate concentration (0.133 mol/kg). The initial water is slightly under-saturated with respect to calcite, with a saturation index of − 0.5; in contrast, the calcite saturation index in the injected water is much lower (− 3.3) due to the lower pH induced by carbonation.

Table 4. Composition of initial water used in the model. The unit of concentration of chemical species is molality (moles per kg water).

Species	Concentration	Species	Concentration	Species
pH	7.91	K	7.10×10^{-5}	Zn
Al	4.45×10^{-6}	Li	6.97×10^{-6}	S(−2)
Ba	4.07×10^{-7}	Mg	5.35×10^{-5}	Cr
Br	8.27×10^{-7}	Mn	1.16×10^{-6}	Se
Ca	7.34×10^{-5}	Mo	4.41×10^{-8}	As
Cd	8.45×10^{-10}	Na	6.70×10^{-3}	N(+5)
Cl	7.31×10^{-4}	Ni	3.41×10^{-8}	Acetic acid (aq)
Co	9.67×10^{-9}	Pb	9.65×10^{-10}	Methane(aq)
Cu	1.73×10^{-8}	S(+6)	1.02×10^{-5}	Ethane(aq)
F	2.40×10^{-5}	Sb	1.33×10^{-8}	Hg
Fe(II)	4.00×10^{-6}	Si	1.75×10^{-4}	Fe(III)
C(+ 4)	6.22×10^{-3}	Sr	1.13×10^{-6}	O_2(aq)[a]
P	3.18×10^{-6}	Na	6.70×10^{-3}	

[a] Computed from redox couple HS^-/SO_4^{-2}.

Chemical reactions considered in the model are aqueous complexation, surface complexation (using a double diffuse layer model), cation exchange (using the Gaines-Thomas convention) and mineral precipitation/dissolution under kinetic constraints (using published rate laws). Aqueous complexes considered in the model are listed in Table A1 in the Appendix. The cation exchange and surface complexation reactions are listed in Table A2, Table A3in the Appendix, respectively. In the current geochemical model, it is assumed that ferrihydrite (as $Fe(OH)_3(s)$) is the adsorbent. The reaction constants for surface complexation of H + and chromium are taken from Dzombak and Morel (1990), for surface complexation reactions of iron and carbonate from Appelo et al. (2002), and for surface complexation on silicate from Jordan et al. (2007).

Based on the mineralogical characterization of the sediment, the model considered illite, smectite, $Fe(OH)_3(s)$ and amorphous iron sulfide (mackinawite, FeS_m), in addition to major aquifer minerals such as quartz, K-feldspar and plagioclase (Table 4). The amount of iron sulfide (FeS_m) was estimated from selective extractions (~ 0.02 vol%), and the amount of $Fe(OH)_3(s)$ from calibration of sediment acid titration simulations (~ 0.135 vol%) as discussed later. Carbonates were not detected using X-ray diffraction (XRD) and solid total inorganic carbon-total organic carbon (TIC-TOC) analysis. However, calcite was found by micro-X ray spectroscopy(Varadharajan et al., 2013). Therefore, trace amounts of calcite were included in the simulations, with an amount calibrated to yield best agreement between simulated and observed metal concentration trends. The amounts of illite, smectite, quartz, and K-feldspar were roughly estimated based on XRD characterization of sediment cores and thin sections (Table 5). Equilibrium constants for these minerals and other secondary phases allowed to form are given in Table 5. These data, as well as dissociation constants for all considered aqueous species (Table A1) were taken from the *Data0.dat.YMPv4.0* EQ3/6 thermodynamic database (Wolery and Jove-Colon, 2007, SNL, 2007). Details on the implemented rate laws and kinetic data for mineral dissolution are given in Appendix A.

Table 5. Equilibrium constants (log(*K*)) and initial volume fraction of minerals in the sediment (on a dry basis). Log(*K*) values are for dissolution reactions that are written with the primary species listed in the first column of Table A1.

Primary mineral	Volume fraction (%)	logK(25 °C)	Potential secondary minerals allowed to form	l
Quartz	94.4	− 3.75	Dolomite	2
Calcite	0.0086	1.85	Siderite	−
FeS_m	0.01	− 3.5	Witherite	1
K-feldspar	2	− 22.39	Rhodochrosite	0
Smectite-Na	0.5	− 38.32	Strontianite	−
Illite	1	− 42.69	Dawsonite	−
$Fe(OH)_3(s)$	0.135	− 5.66		
Ab80An20	2	− 14.8		

3.4. pH buffering capacity

Sediment titrations were conducted to evaluate the pH buffering capacity of the aquifer (Varadharajan et al., 2013). A mixture of 1 g sediment and 5 ml deionized water was titrated with a 0.01 M HCl solution. Simulations of these sediment acid titrations were used to constrain pH buffering reactions implemented in the reactive transport model. These reactions were assumed to consist primarily of surface protonation/deprotonation reactions, as well as the dissolution of carbonate minerals (calcite). However, the simulations showed that the calcite amount in the sediments (Table 5) was too small to significantly buffer pH upon acid titration. This implies that, for these sediments, the pH buffering behavior was dominated by H^+ adsorption. To model such adsorption, protonation/deprotonation reaction equilibrium constants and sorption site densities were taken from Dzombak and Morel (1990), assuming that H^+ adsorption occurs dominantly onto ferric iron (oxy)hydroxides (here modeled as ferrihydrite in the form of $Fe(OH)_3(s)$). Using these data, the volume fraction of $Fe(OH)_3(s)$ in the sediment was then calibrated (0.135%) to best reproduce the titration curve obtained for sample PW-1-160 that is representative of the aquifer sandy sediment (Fig. A1 in electronic supplementary information (ESI)).

4. Modeling results

Results of various simulations are presented below and organized as follows. First, results of a “base case” model are presented. This model implements the metal release reactions postulated in Table 2, with focus on simulated trends of pH, alkalinity, and concentrations of alkali and alkaline earth metals, Ba, Fe, Si and Cr. In a second part, we then evaluate the sensitivity of modeling results to a variety of key parameters and processes such as surface protonation, calcite dissolution, and cation exchange capacity (CEC). Finally, we also explore conceptual model variations to help explain some of the discrepancies between observed metal concentration trends and the base-case model results.

4.1. Base-case model

4.1.1. pH and alkalinity

Groundwater pumped out from PW-1 is saturated with CO_2 at the surface and then injected through IW-1. The dissolved CO_2 dissociates into bicarbonate and protons ($CO_2 + H_2O \rightleftharpoons HCO_3^- + H^+$), which increases the total dissolved inorganic carbon content (DIC) and decreases pH in the impacted groundwater. This carbonated water displaces the groundwater in the aquifer, spreads out from IW-1 towards PW-1, and forms a plume of elliptic shape that is high in DIC and low in pH, as illustrated by the simulated spatial distribution of pH at several time points (Fig. 6a and b). The center of the plume has a pH of around 5; the edge of the plume a pH between 5 and 8 caused by dispersion and buffering of the acidic plume by chemical reactions. Low-pH groundwater arrives first at MW-3, then at MW-2 and MW-1. At the end of the injection/pumping period (i.e., 156 days after the injection and pumping started), low-pH groundwater arrives at MW-4 (Fig. 6c). Once injection/pumping ends, because of the stagnant regional groundwater flow, the plume remains at the same location, however, the pH value at the center of the plume increases gradually.

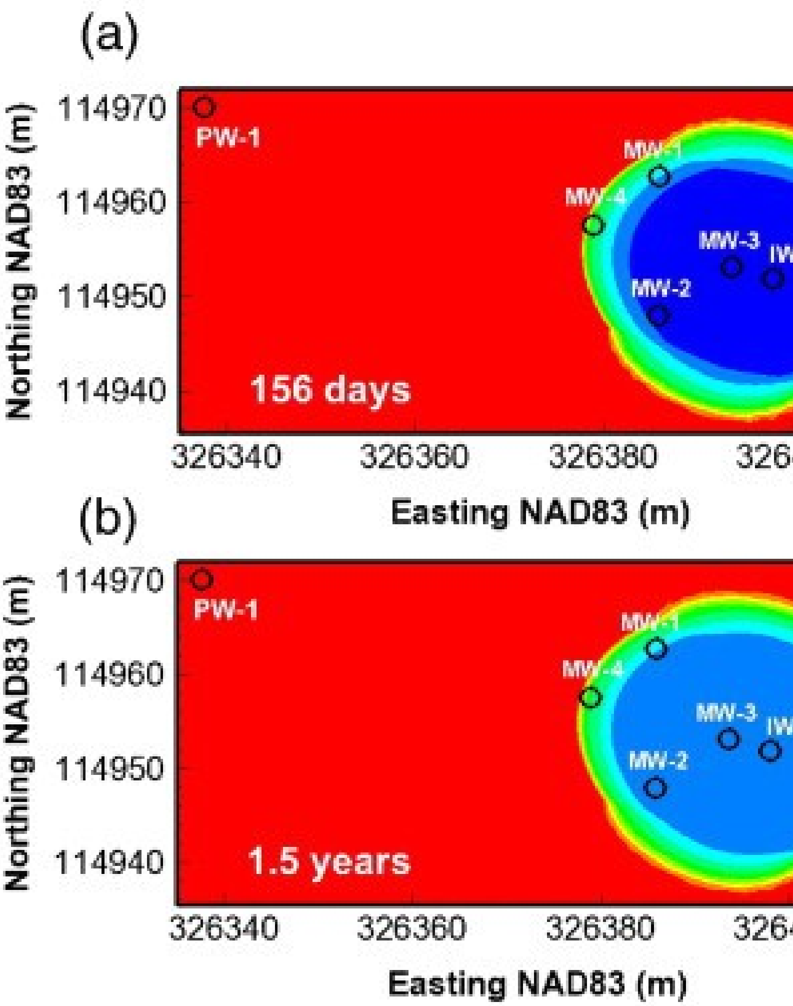

1. Download high-res image (716KB)
2. Download full-size image

Fig. 6. Simulated spatial distributions of pH at 156 days (a) and 1.5 years (b), and simulated and observed breakthrough curves of pH (c) at monitoring wells MW-1, MW-2, MW-3, and MW-4.

Modeling results for groundwater pH match measured data reasonably well, but some discrepancies are observed (Fig. 6c). For example, the pH at MW-4 started to drop earlier in the model compared to what was observed in the field. Furthermore, at other well locations the modeled pH does not rebound fast enough to match the recovery exhibited in the field. A change in dissolved CO_2 concentration is just one of many processes that can affect groundwater pH. Other processes include the dissolution of calcite and plagioclase, and surface complexation. Sensitivity analyses reported later in this paper illustrate how these processes affect the simulated spatial and temporal evolution of pH. Fig. 7a and b show the modeled spatial distribution of alkalinity at two time-points. Given the high-DIC concentrations during injection and the simulated pH conditions of the plume, bicarbonate (HCO_3^-) is the dominant component of total alkalinity, with much lower concentrations of carbonate (CO_3^{-2}). Hence, the simulated alkalinity values are taken as the sum of the predicted concentrations of HCO_3^- and CO_3^{-2}. Unlike the plume of DIC and pH, the plume of bicarbonate is shaped like a donut—higher concentrations at the moving edge of the plume but very low concentration in the center, which is caused by the dominance of carbonic acid ($H_2CO_3^0$) once the pH drops below about 6.

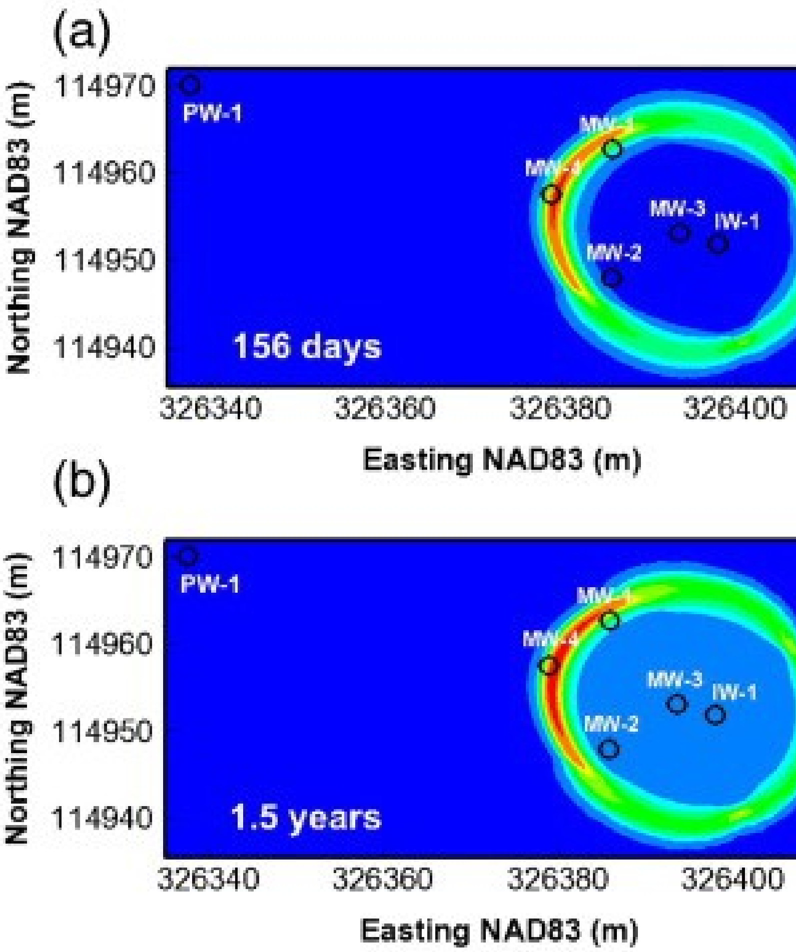

1. Download high-res image (636KB)
2. Download full-size image

Fig. 7. Simulated spatial distributions of alkalinity at 156 days (a) and 1.5 years (b), and simulated and observed breakthrough curves of alkalinity (c) at monitoring wells MW-1, MW-2, MW-3, and MW-4.

The modeled alkalinity values are compared with the measured total alkalinity trends in Fig. 7c. As the plume passes the monitoring wells, the temporal evolution of alkalinity shows a pulse-like shape initially, followed by a slow recovery after CO_2 injection and pumping stopped. This trend is clearly observed at MW-1, MW-2 and MW-3, but less pronounced at MW-4. Computed and measured breakthroughs of alkalinity are similar at MW-3, but only show qualitative and not quantitative agreements at other wells. The major discrepancy between model results and field data is that the computed peak heights of alkalinity breakthrough curves*increase* for wells further away from IW-1, while the observed peak heights *decrease* with longer distances away from IW-1. This type of discrepancy persists for breakthrough curves of most dissolved species, as discussed later.

4.1.2. Alkali and alkaline earth metals

The increase in carbonate content and the drop of pH trigger the dissolution of two calcium-bearing minerals: calcite and Ab80An20 (a plagioclase with 80% albite and 20% anorthite). The former dissolves much faster than the latter. The current model calibration indicates that the amount of calcite is fairly small and would be depleted shortly after the arrival of acidified water. The dissolution of a limited amount of calcite creates a donut-shape plume of Ca as shown in Fig. 8a and b. Regarding the breakthrough curves of Ca at the four monitoring wells (Fig. 8c), two concentration trends can be observed: (1) a pulse-like temporal change characterized by a rise in Ca concentrations upon the arrival of acidified water followed by a decrease in concentrations until the end of CO_2 injection (“pulse period”), and (2) a bounce-back of Ca concentration levels during the post-injection period (“recovery period”).

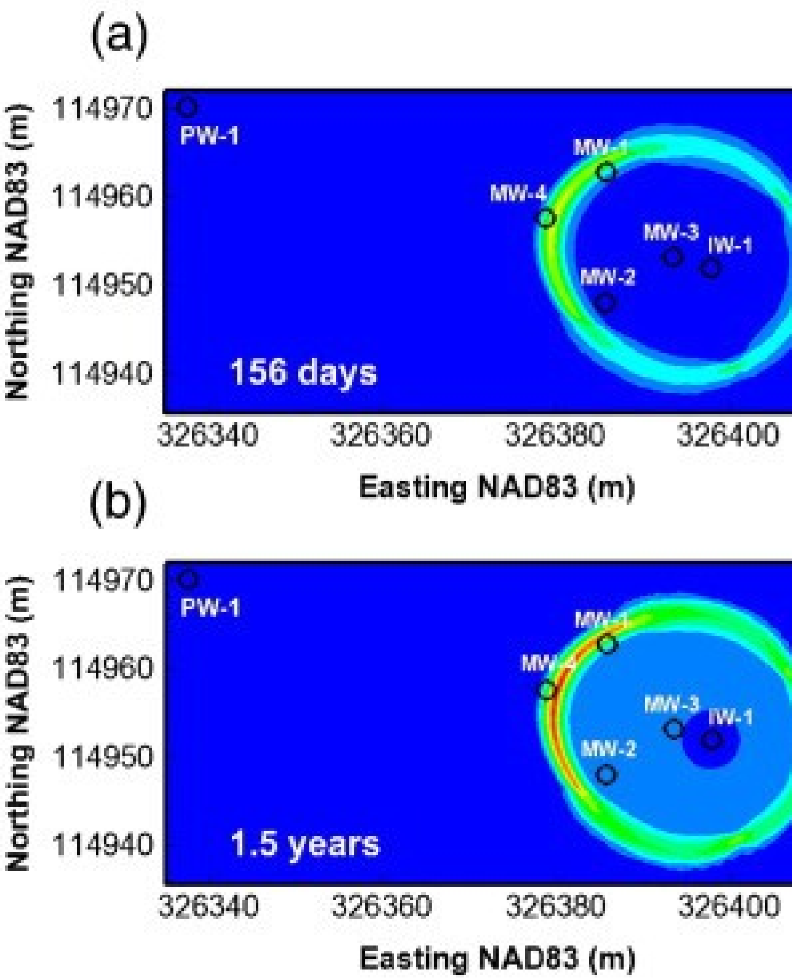

Fig. 8. Simulated spatial distributions of total dissolved Ca (“t_ca + 2”) at 156 days (a) and 1.5 years (b) after the beginning of CO_2 injection, and Ca breakthrough curves (c) at monitoring wells MW-1, MW-2, MW-3, and MW-4.

This evolution of Ca at MW-3 was interpreted by Zheng et al. (2015) with a model concept that encompasses (a) a fast-reacting but limited pool of reactive minerals that respond quickly to changes in pH and can explain the pulse period, and (b) a slow-reacting but essentially unlimited mineral pool to yield rising concentrations upon decreased groundwater velocities after pumping and injection stopped in the recovery period. This conceptualization combines the initial fast pulsing behavior with transport-limited kinetic dissolution trends (e.g., Johnson et al., 1998) that are strongly dependent on groundwater residence times. Under these conditions, rising metal concentrations from the dissolution of minerals are only noticeable when the groundwater velocity is slow (relative to the reaction rate) or inversely when reaction rates are fast (relative to the groundwater velocity). For Ca, the fast-reacting but limited pool is the dissolution of a limited amount of calcite (~ 0.009% in volume fraction), and the slow-reacting but essentially unlimited pool is the dissolution of plagioclase. The close match between the computed and measured breakthrough curves of Ca at MW-3 support this concept. Model results at other wells, however, fail to quantitatively reproduce the measured data, although qualitatively they exhibit similar trends. Similarly to alkalinity, the most noticeable discrepancy between modeled and measured data is that the computed breakthroughs at the four monitoring well show increasingly higher peaks with distance from the injection well (IW-1), during the “pulse period”, whereas measured breakthroughs at these four monitoring wells show increasingly lower peaks as the plume moves further away from IW-1.

The release of Ca into solution triggers a series of cation exchange reactions that lead to the increase in concentrations of major elements such as Na, K, Mg, Mn, and trace elements such Ba, Sr, and Li. This explains why the concentrations of these elements exhibit trends parallel to Ca (e.g. see Fig. 9a for barium as example). Because cation exchange reactions are fast (relative to mineral dissolution), the temporal evolution of concentrations for these elements (Sr, Li, Na, K, Mg and Mn; Figs. A2 to A7 in ESI) is quite similar to that of Ca. The best fits of measured data with model results are achieved for Ba, Sr, Li, and Mg, and the matches between measured and computed values are not as good for Na, K and Mn. The deviations between measured and computed concentrations of Ca at wells other than MW-3 are similar to deviations observed for Ba, Sr, Li, Na, K, Mg and Mn.

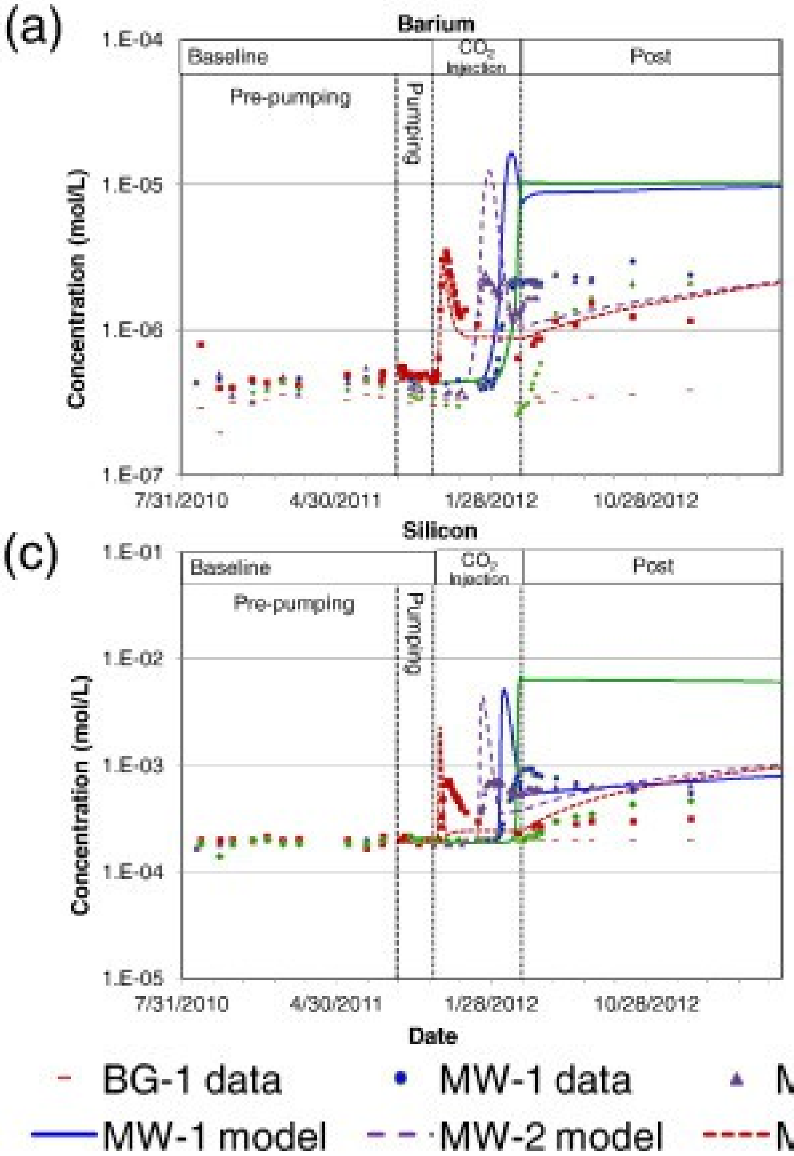

Fig. 9. Simulated and observed breakthrough curves of total Ba (a), Fe (b), Si (c), and Cr (d) concentrations at monitoring wells MW-1, MW-2, MW-3, and MW-4.

4.1.3. Iron

Measured total Fe concentrations (essentially all Fe(II) within the observed pH range) exhibit similar spatial and temporal distributions as Ca. However, for Fe, the fast-reacting (limited) pool is modeled as the desorption of Fe(II) from the surface of $Fe(OH)_3$(s), and the slow-reacting (unlimited) pool as the dissolution of iron sulfide. This concept leads to a fair fit between measured and computed data at MW-3 (Fig. 9b). However, the initial modeled pulse is much narrower than observed, and with a higher peak than the measured data. This discrepancy may be the result of assuming equilibrium surface complexation reactions. Surface complexation reactions are typically quite fast, ranging from days to weeks, such that these reactions can often be treated as an equilibrium process for the simulation of subsurface systems over the long term. However, in the present case, this assumption may yield a Fe pulse at MW-3 that is too short in time (lasting only a few weeks). As soon as the injection/pumping stops, the simulated concentration of Fe increases, which is modeled here with reasonable results (Fig. 9b) by the dissolution of iron sulfide. The pH decrease resulting from the introduction of CO_2 in the subsurface could also induce a greater rate of microbial Fe(III) reduction (Kirk, 2011, Kirk et al., 2013). This could not be ruled out as another mechanism leading to increased Fe(II) concentrations in groundwater, also it would not be expected to be the cause of the initial short-lived Fe(II) pulse observed in the field. It should also be noted that the modeled and measured Fe breakthrough curves at MW-1, MW-2 and MW-4 only match qualitatively but not quantitatively.

4.1.4. Silicon

The spatial and temporal evolution of Si (Fig. 9c) is similar to that of Ca and Fe. Therefore, in the base case model, release mechanisms similar to those proposed for Ca and Fe are used to explain the behavior of Si: the fast-reacting (limited) pool for Si is driven by Si desorption from $Fe(OH)_3(s)$ surfaces, and the slow-reacting (unlimited) pool is represented by the dissolution of plagioclase (Ab80An20). This concept explains qualitatively the first “pulse period” and the following “recovery period” exhibited in the breakthrough curves of Si at MW-1, MW-2 and MW-3, but results in similar departures as for other species— moving further away from IW-1, the peaks of the computed breakthrough curves at the four monitoring wells keep increasing, in contrast to the measured breakthrough peaks, which continue decreasing.

4.1.5. Chromium

Cr appears to behave slightly differently from other metals. The breakthrough of Cr at MW-3 is similar to that of other elements, i.e. an initial “pulse period” is followed by a “recovery period” after injection stopped (Fig. 9d). But such a trend is not observed for the Cr breakthrough curves at other wells. Cr breakthrough curves at MW-1 and MW-2 only show an initial rising and falling, but no further concentration increase during the recovery period. Cr concentrations at MW-4 are below the detection limit. The model that considers desorption of Cr matches somewhat the measured Cr at MW-3 but not the observed behavior at other wells.

4.2. Sensitivity of model results to input parameters and modeled processes

In this section, we explore the sensitivity of model results to key parameters and reactive processes, trying to shed light on how these processes affect the modeled concentration trends of dissolved major and trace elements as a result of the injection of CO_2-bearing water. These sensitivity analyses are by no means exhaustive and are only intended to show the effect of presumed key input parameters (or particular types of reactions) on model results. To do so, for each sensitivity case, only the model inputs being tested are varied, while the rest of the parameters and reactions remain the same as in the base-case model.

4.2.1. The impact of surface complexation on modeled pH

Many reactions can affect groundwater pH, including the pH buffering by the dissolution of calcite (or other carbonate minerals) (e.g. Carroll et al., 2009) and surface protonation reactions (e.g. Zheng et al., 2009, Zheng et al., 2012; Table A3). Another pH-buffering surface reaction that was not considered in these earlier studies is the surface adsorption/desorption of bicarbonate (Appelo et al., 2002). The dominant of these surface complexation reactions can be written as (Table A3):

(1)$\mathrm{HFO\_wOH_2^+ = HFO\_wOH + H^+}$

(2)$\mathrm{HFO\_wCO_2H + H_2O \rightleftharpoons HFO\_wOH + HCO_3^- + H^+}$

In the base-case model, the volume fraction of calcite was found to be too small for calcite to buffer pH significantly. Hence, (1), (2) are the main reactions that buffer pH. We conducted two sensitivity analyses to illustrate how these two reactions affect the temporal changes of pH: Model “A” does not consider surface complexation of bicarbonate and Model “B” considers neither surface protonation nor surface complexation of bicarbonate. In comparison with the base-case model, Model A leads to an earlier breakthrough of pH, lower pH values, and slightly higher total dissolved carbonate concentrations, with increasingly noticeable differences away from MW-1 (Fig. 10a and b). Similar but more pronounced differences from the base-case model are predicted if neither surface protonation nor surface complexation of carbonate is considered (Model B) (Fig. 10c and d). The earlier breakthrough of pH with models A and B leads to an earlier rise of Ca and trace metalsconcentrations, which does not fit the measured data as well as the base-case model. It is however noteworthy to mention that these observations are based on specific surface complexation reactions and equilibrium sorption constants (Dzombak and Morel, 1990, Appelo et al., 2002), together with the assumption that $Fe(OH)_3(s)$ is the dominant adsorbent with an amount calibrated based on sediment titration data (Section 3.4)— Changing any of these model conditions might change the model results described above.

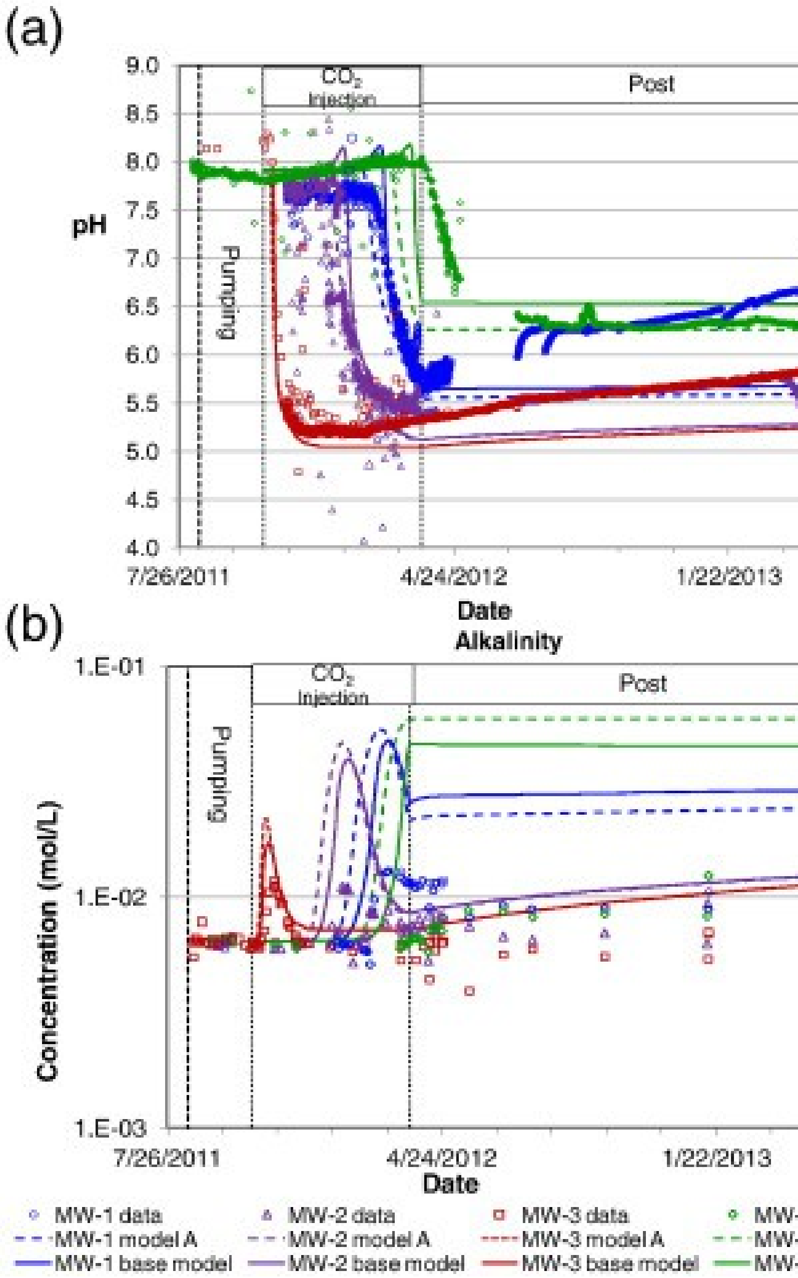

1. Download high-res image (990KB)
2. Download full-size image

Fig. 10. Simulated and observed breakthrough curves at MW-1, MW-2, MW-3 and MW-4, comparing the base-case model with Model A (no HCO_3^- surface complexation) for pH (a) and alkalinity (b), and with Model B (no H + and no HCO_3^- surface complexation) for pH (c) and alkalinity (d).

4.2.2. Sensitivity to calcite volume fraction and dissolution rate

In the geochemical model presented here, the calcite dissolution rate and the abundance of calcite play the key role in determining the responses of most major and trace elements, especially during the initial “pulse period” of the breakthrough curve. This is because alkali and alkaline earth metal are released via cation exchange, which is directly driven by the amount of Ca released by calcite dissolution (in other words, increasing the amount of calcite in the model enhances the release of Ca and other metals). In this sensitivity analysis, the calcite effective dissolution rate (*r* in Eq. (A1)) was increased by raising the specific surface area of calcite by two orders of magnitude. When doing so, the higher calcite dissolution rate has an insignificant impact on pH (Fig. A9 in ESI), but leads to a higher peak value and narrower span of the initial Ca concentration pulse (Fig. 11a and b). The higher dissolution rate also leads to a faster depletion of calcite. The resulting changes in trace metal (Ba, Mg, Mn, K, Li, Na and Sr) concentrations (see Fig. 11b using Ba as an example) follow the Ca trend, because the change in Ca concentration is the driving force for the concentration changes in other trace metals.

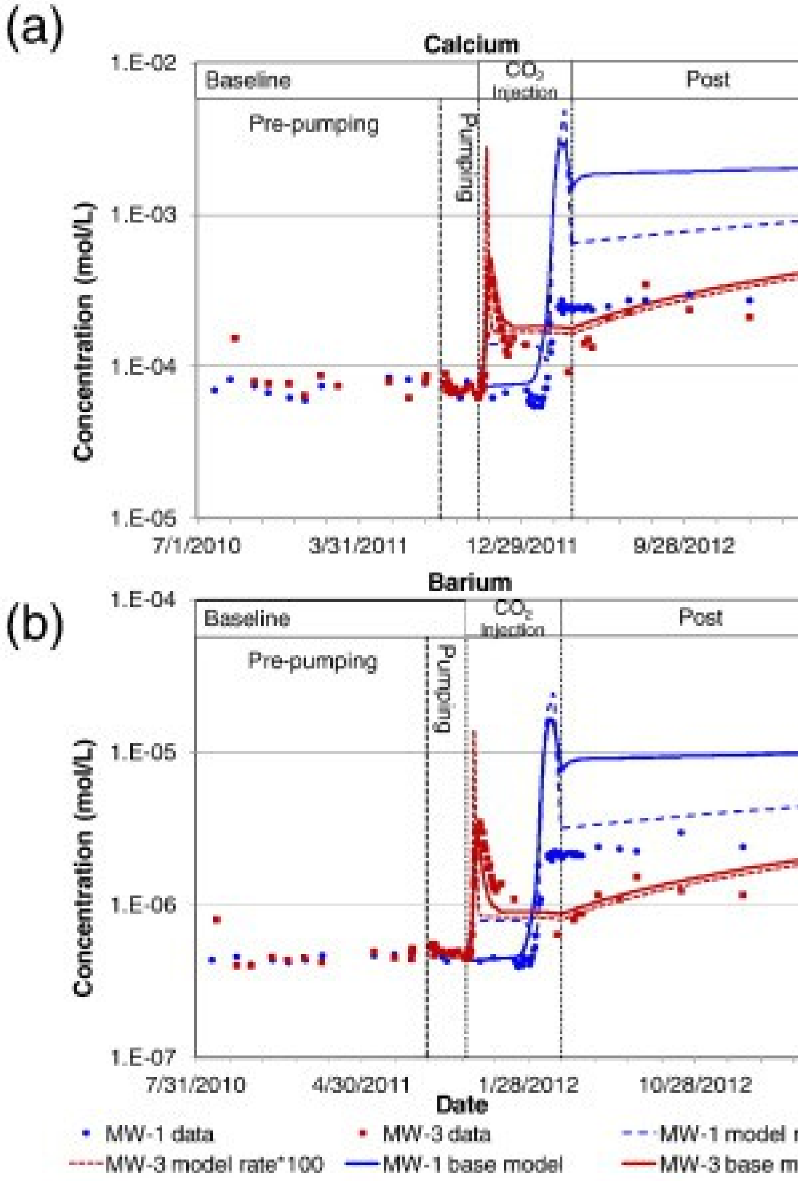

Fig. 11. Computed breakthrough curves at MW-1 and MW-3 for Ca (a) and Ba (b) after increasing the specific surface are of calcite (Eq. (A1)) by two orders of magnitude, and for Ca (c) and Ba (d) after increasing the initial calcite volume fraction by a factor of ten reactive to the base-case model.

The current model relies on the dissolution and the subsequent depletion of a limited amount of calcite to explain the pulse-like behavior in the breakthrough of Ca and some major and trace elements. In the base case, the volume fraction of calcite was calibrated yielding a quite a small amount (8.6×10^{-5}, dimensionless units), which is well below XRD detection limits. Fig. 11c shows model results for a sensitivity analysis with a calcite volume fraction that is 10 times higher. The higher initial volume fraction of calcite results in a higher Ca concentration peak, a wider span of the pulse, and also in higher Ca concentrations during the recovery period. The concentration profiles of alkali and alkaline earth metals are affected in a similar manner by the increased amount of calcite because their profiles follow that of Ca (see Fig. 11d for Ba as an example). The higher initial volume fraction of calcite also leads to a much delayed breakthrough of pH (see Fig. A10 in ESI).

4.2.3. Sensitivity to cation exchange capacity (CEC)

The base-case model relies on cation exchange reactions to explain the changes in concentration of Ba, Mg, Mn, K, Li, Na and Sr. Here we vary the CEC value input in the model to examine the effect of CEC on the concentration of relevant species. Fig. 12ashows the breakthrough curve of Ca at MW-1 and MW-3 calculated using CEC values that are either twice as large, or half of the value used in the base-case model. Larger CEC values result in more Ca residing in exchangeable sites. Therefore, the concentration of Ca in the aqueous phase is lower at larger CEC values (Fig. 12a). Conversely, it is higher at lower CEC values as less Ca is partitioned on exchangeable sites (Fig. 12a). Larger CEC values also mean that exchange sites would retain more trace metals in the solid phase and therefore lead to lower concentration of trace metals in aqueous phase, as exemplified with Ba (Fig. 12b).

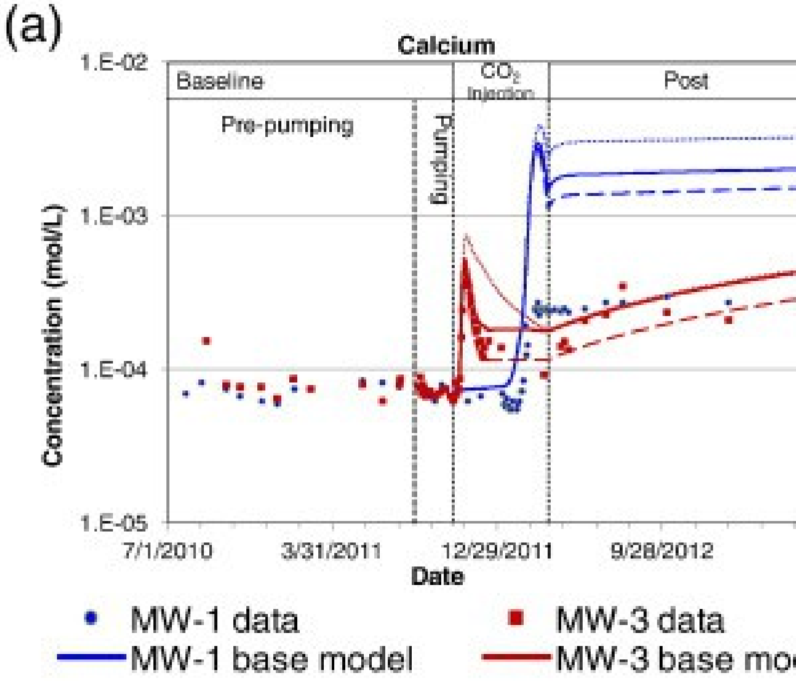

Fig. 12. Sensitivity of the breakthrough curves of Ca (a) and Ba (b) at MW-1 and MW-3 to CEC value, while testing CEC values that are either twice as large (“CEC*2”) or half of the value (“CEC/2”) initially used in the base-case model.

4.2.4. The effect of cation exchange on iron concentrations

In the base case, the desorption of Fe from $Fe(OH)_3$(s) surfaces is used to interpret the initial pulse shown in the breakthrough curve of Fe. One question, however, is whether Fe could be rather present in exchangeable surface sites, thus whether cation exchange is rather the process that leads to the increase in Fe concentrations. In order to test this hypothesis, we conducted a simulation (Model C in Fig. 13a) in which Fe(II) was included as an exchangeable cation and excluded from sorption sites. With this conceptual model, the release of Fe via cation exchange with Ca is responsible for the initial pulse of Fe. Fig. 13a shows the model results of this simulation, using exchange equilibrium constants for Fe(II) from Appelo and Postma (1994). In this case, the computed Fe concentrations are much lower than measured concentrations, therefore suggesting that exchangeable Fe alone does not provide a high enough Fe source.

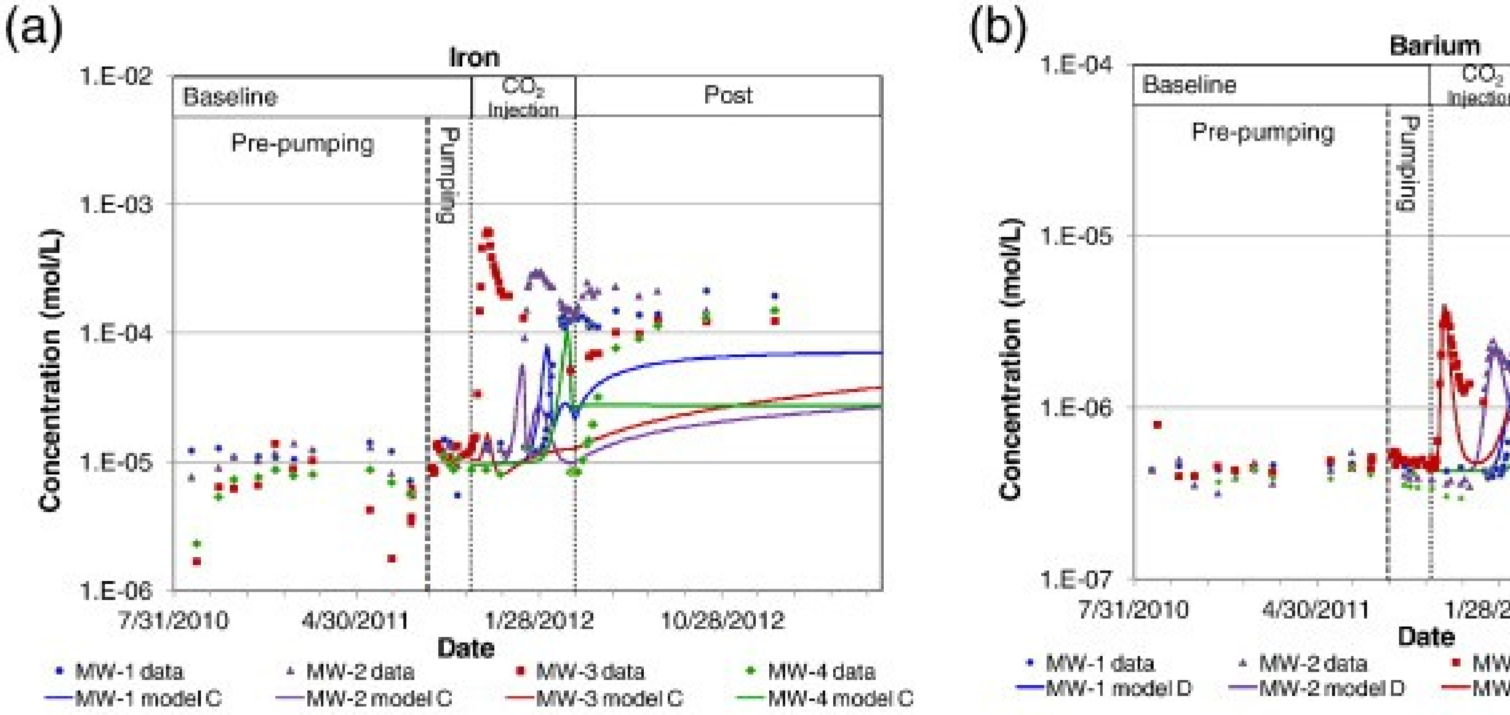

1. Download high-res image (433KB)
2. Download full-size image

Fig. 13. Model sensitivity to different modeling concepts: (a) Fe at monitoring wells MW-1, MW-2, MW-3, and MW-4 for a simulation (Model C) in which Fe(II) is included as an exchangeable cation while excluding Fe desorption from $Fe(OH)_3$(s) surfaces (compare with Fig. 9b); (b) Ba at monitoring wells MW-1, MW-2, MW-3, and MW-4 computed with a model (Model D) considering increased trace metal release in the vicinity of the injection well (MW-3) (compare with Fig. 9a).

Table A3. Surface complexation reactions and surface complexation constants (logK) on ferrihydrite (double diffuse layer model) (Dzombak and Morel, 1990, Appelo et al., 2002, Jordan et al., 2007).

Surface complexation
$HFO\_sOH_2^+ = HFO\_sOH + H^+$
$HFO\_wOH_2^+ = HFO\_wOH + H^+$
$HFO\_sO^- + H^+ = HFO\_sOH$
$HFO\_wO^- + H^+ = HFO\_wOH$
$HFO\_sOFe^+ + H^+ = HFO\_sOH + Fe^{+2}$
$HFO\_wOFe^+ + H^+ = HFO\_wOH + Fe^{+2}$
$HFO\_wOFeOH + 2H^+ = HFO\_wOH + Fe^{+2} + H_2O$

injection well is screened beyond the interval of the sandy aquifer, the injected carbonated water could infiltrate the top and bottom clay layers near the injection well and sweep off some trace elements therein and carry them into the aquifer. Another possibility is simply that the clay content of the aquifer near the injection well could be higher than at other locations due to local heterogeneity. Without resorting to a 3D model, these cases can be tested by either increasing the cation exchange capacity near the injection well, or by increasing the calcite volume fraction in this area, as long as the calcite amount remains low enough to drive more cation exchange (by Ca dissolution) without significantly affecting pH. For simplicity we chose the latter (Model D in Fig. 13b), and increased the volume fraction of calcite to 3.5×10^{-4} (dimensionless units) within a 4-m radius area around the injection well. Note that the total amount of calcite relative the affected area in the aquifer is still too small to have a noticeable effect on the magnitude of pH drop. Because the amount of metals loaded onto exchangeable sites is large enough to account for the observed released concentrations, the amount of exchangeable Ca produced by calcite dissolution is the main factor limiting the release of these metals. Therefore, increasing the volume fraction of calcite near the injection well is equivalent to increasing the source of metals at this location. Fig. 13b shows the model results for Ba when applying this concept (similar results for Ca are shown in Fig. A11 in ESI). In comparison to the base-case model, this case leads to overall better matches of the measured data at MW-1, MW-2 and MW-4, but to a somewhat worse fit of the data at MW-3. Although this concept leads to slightly worse fit of pH breakthrough (Fig. A12 in ESI), the overall better match between measured and simulated data for this case suggests that the top and bottom clay formations near the injection well, or a generally increased amount of exchangeable metals at this location (from heterogeneous distribution of clay minerals), could explain the observed decreasing pulse intensity of dissolved metals concentrations away from the injections well.

5. Summary and conclusions

A controlled release field test was conducted with an extensive water quality monitoring program during and after the injection of carbonated water, to mimic the effect of a potential leak of $CO_2$from a deep storage site to a shallow aquifer. This field test provided a great opportunity to evaluate and model potential reactive mechanisms responsible for the release of metals in groundwater and strengthen our understanding of the hydrogeological and chemical processes relevant to potential impacts on groundwater quality at CO_2 geological sequestration sites. Reactive transport models have been developed to interpret the concentration changes observed at four monitoring wells during the field test. The breakthrough curves of major and trace elementsat these monitoring wells show a pulse-like change during the carbonated water injection period, followed by slowly increasing concentration levels during the post-injection period. A reasonable match between model results and field data indicate that this trend can be interpreted with a conceptual model that considers (a) a fast-reacting but limited pool of reactive minerals that respond quickly to changes in pH, to explain the pulse-like changes in metal concentrations, and (b) a slow-reacting but essentially unlimited mineral pool that yields rising concentrations upon decreased groundwater velocities after pumping and injection stopped.

For Ca, Ba, Mg, Mn, K, Li, Na and Sr, a reasonable agreement of model results with observed data was obtained when the fast-reacting but limited pool was modeled as calcite dissolution and Ca-driven cations exchange reactions, and the slow-reacting but unlimited pool was modeled as the dissolution of plagioclase and longer-term Ca-driven cation exchange. For Fe, best results were obtained when modeling fast desorption from iron hydroxides($Fe(OH)_3(s)$) together with slow dissolution of amorphous iron sulfide; similarly, good results for Si were obtained by considering fast desorption of Si from iron hydroxides concomitant with slow dissolution of plagioclase. In our modeling study, small finite amounts of fast-dissolving calcite were assumed to be the source of the initial Ca pulse, although it should be noted that finite amounts of Ca and/or Mg desorbing from organics or hydroxides would be expected to yield a similar pulse behavior.

A series of sensitivity analyses demonstrated that the initial calcite volume fraction, calcite dissolution rate and CEC value of the sediments are critical parameters to model the temporal changes in concentrations of Ca, Ba, Mg, Mn, K, Li, Na and Sr. The regional groundwater flow affects not only the time of breakthrough but also the concentration levels during the post-injection period. This is because the groundwater residence time, which is inversely proportional to flow rate, has a direct effect on extent of reaction, thus slow mineral dissolution becomes noticeable only under slow flow rates (large residence times).

The most noticeable discrepancy between modeled and observed breakthrough curves is that computed breakthroughs at the four monitoring wells show increasing pulse peak concentrations at wells further away from the injection well (IW-1). In contrast, the observed breakthrough at four monitoring wells show the reverse behavior, with decreasing peak heights of breakthrough curves at larger distances away from IW-1. This discrepancy is reduced when chemical spatial heterogeneity is considered in the model. Essentially, the observed decreasing pulse peaks away from the injection well can be reproduced by modeling a larger initial source of Ca and/or trace elements near the injection well than farther away from it. This source term could result of carbonated water contacting clays (such as the top and bottom aquitards near the injection well), or simply a more abundant fast-release source of Ca (calcite, or possibly Ca-adsorbing organic matter and/or hydroxides) near the injection well. Overall, this study further demonstrates the importance of thorough field geochemical and hydrological characterization for environmental risk assessments, covering both the CO_2 injection and post-injection time-periods at CO_2 sequestration sites, and considering the important effect of groundwater flow rate (residence time) on the magnitude of released metal concentrations.

Acknowledgement

This work was supported by the Electric Power Research Institutevia contract WF006458AMD1 with LBNL the EPA, Office of Water, under an Interagency Agreement with the U.S. Department of Energy (DOE) at LBNL, under contract number DE-AC02-05CH11231; and the Assistant Secretary for Fossil Energy, National Energy Technology Laboratory (NETL), National Risk Assessment Program (NRAP), of the US Department of Energyunder Contract No. DEAC02-05CH11231.

Appendix A.

Table A1. List of aqueous complexes used in the model and log(*K*)'s for reactions that are written with the primary species listed the first column.

Primary species	Aqueous complex	logK(25 °C)	Aqueous complex	logK(25 °C)
H^{+}	ClO_2^{-}	23.107	$CaCO_3(aq)$	7.009
H_2O	HSO_5^{-}	17.29	$CaCl^{+}$	0.297
AlO_2^{-}	$S_2O_3^{-2}$	133.549	$CaCl_2(aq)$	0.654
Ba^{+2}	SO_3^{-2}	46.625	$CaHCO_3^{+}$	− 1.043
Ca^{+2}	$Al(SO_4)_2^{-}$	− 27.104	$CaOH^{+}$	12.834
Cl^{-}	$Al_{13}O_4(OH)_{24}$	− 189.919	$CaSO_4(aq)$	− 2.1
Fe^{+2}	$Fe_{13}O_4(OH)_{24}$	58.85	$Fe(CO_3)_2^{-2}$	13.498
HCO_3^{-}	$Al_2(OH)_2^{+4}$	− 36.717	$Fe(OH)_3^{-}$	31
K^{+}	$Al_3(OH)_4^{+5}$	− 52.731	$Fe(OH)_4^{-2}$	46
Li^{+}	$Al_2(OH)_2CO_3^{+}$	− 38.721	$Fe(SO_4)^{2-}$	− 3.214
Mg^{+2}	$Al_3(OH)_4HCO_3$	− 58.025	$Fe_2(OH)_2^{+4}$	2.95
Mn^{+2}	$Fe_2(OH)_2CO^{3+}$	0.627	$Fe_3(OH)_4^{+5}$	6.3
Na^{+}	$Fe_3(OH)_4HCO_3$	0.986	$FeCO_3(aq)$	4.879
SO_4^{-2}	AlO^{+}	− 11.857	$FeCl^{+}$	0.165
$SiO_2(aq)$	Al^{+3}	− 22.199	$FeCl^{+2}$	− 1.475
Sr^{+2}	$AlOH^{+2}$	− 17.2	$AlCl^{+2}$	− 21.685
Zn^{+2}	$AlSO_4^{+}$	− 25.214	$FeCl_2(aq)$	8.181
HS^{-}	$BaCO_3(aq)$	7.691	$FeHCO_3^{+}$	− 1.47
Fe^{+3}	$BaCl^{+}$	0.503	$FeO(aq)$	20.412
$O_2(aq)$	$BaHCO_3^{+}$	− 1.012	$MgO(aq)$	24.491
	$BaOH^{+}$	13.502	$CaO(aq)$	24.851
	$CO_2(aq)$	− 6.341	FeO^{+}	5.652

Primary species	Aqueous complex	logK(25 °C)	Aqueous complex	logK(25
	CO_3^{-2}	10.325	FeO_2^-	21.618

Table A2. Cation exchange reactions and selectivity coefficients, using the Gaines-Thomas convention (Appelo and Postma, 1994).

Cation exchange reaction
$Na^+ + X - H = X - Na + H^+$
$Na^+ + X - K = X - Na + K^+$
$Na^+ + 0.5X - Ca = X - Na + 0.5Ca^{+2}$
$Na^+ + 0.5X - Mg = X - Na + 0.5\ Mg^{+2}$
$Na^+ + 0.5X - Ba = X - Na + 0.5Ba^{+2}$
$Na^+ + 0.5X - Mn = X - Na + 0.5Mn^{+2}$
$Na^+ + 0.5X - Sr = X - Na + 0.5Sr^{+2}$
$Na^+ + X - Li = X - Li + Li^+$

A general form of rate law is implemented for the dissolution and precipitation of solid phases (Lasaga et al., 1994):

(A1)$r=kA1-KQ\theta\eta$

where *r* is the kinetic rate, *k* is the rate constant (mol/m^2/s) which is temperature dependent, *A* is the reactive surface area per kg water, *K* is the equilibrium constant for the mineral–water reaction written for the dissolution of one mole of mineral, and *Q* is the ion activity product of the dissolution reaction. Here, for simplicity, the exponents θ and η are assumed to be equal to 1. *A* is a function of the mineral specific surface area (e.g., cm^2/g mineral), the volume fraction and density of each mineral in the sediment, and porosity.

The rate constant for calcite dissolution is given as a combination of neutral, acid and carbonate mechanisms (Plummer et al., 1979):

(A2)$kc=1.5\times10-6e-Eanu/RT+0.5e-EaH/RTaH+9.6\times10-5e-EaCO2/RTaCO2$

where E_a^{nu}, E_a^H and E_a^{CO2} are activation energies with values of 23.5, 14.4 and 35.4 (kJ/mol), respectively. The rate constant for the neutral, acid and carbonate mechanisms, are respectively 1.5×10^{-6}, 0.5 and 9.6×10^{-5}. a_H is the H$^+$ activity and a_{CO2} is the activity of dissolved CO$_2$. In the model, the specific surface area of calcite (9.8 cm^2/g) was calibrated, together with the initial calcite volume fraction, to match the breakthrough of observed alkaline earth metals concentrations of Ca, Ba and Sr in MW-3. Assuming spherical grains, the value of the calibrated surface area would correspond to the geometric surface area of millimeter-sized grains. Because the product of the specific surface area and volume fraction is of relevance to the reaction rate (not each value individually), calibrated values of specific surface area or volume fraction should be viewed as non-unique (co-linearly varying) values. The specific surface areas and kinetic rates of minerals other than calcite are listed in Table A4. Most rate constants were taken from Palandri and Kharaka (2004). The dissolution rate constant of plagioclase (Ab80An20) was calibrated based on Ca concentration changes observed at MW-3. The rate constant is higher than that of albite but lower than that of anorthite (Palandri and Kharaka, 2004). The rate constant for FeS_m was taken from Pankow and Morgan (1980). Specific surface areas for most minerals were arbitrarily set to the same value as for calcite, except for FeS_m, for which the surface area was increased (56 cm^2/g) to match Fe concentrations at MW-3.

Table A4. Kinetic properties for minerals considered in the model (see text for sources).

Mineral	A (cm^2/g)	Parameters fo		
		Neutral mechanism		Acid me
		k_{25} (mol/m^2/s)	E_a (KJ/mol)	k_{25}
Primary				
Quartz	9.8	1.023×10^{-14}	87.7	
K-feldspar	9.8	3.89×10^{-13}	38	8.71×10^{-11}
Ab80An20	9.8	1.95×10^{-12}	65	2.95×10^{-4}
Kaolinite	9.8	6.91×10^{-14}	22.2	4.89×10^{-12}
Smectite-Ca	9.8	1.66×10^{-13}	35	1.05×10^{-11}
Illite	9.8	1.66×10^{-13}	35	1.05×10^{-11}
Fe(OH)$_3$(s)	9.8	2.51×10^{-15}	66.2	8.7×10^{-11}
FeS_m	56.0	3.27×10^{-7}	0	

Mineral	A (cm^2/g)	Parameters for kinetic rate law		
		Neutral mechanism		
		k_{25} ($mol/m^2/s$)	E_a (KJ/mol)	
Secondary				
Gypsum	9.8	1.62×10^{-3}	0	
Dolomite	9.8	2.51×10^{-9}	95.3	1.74 ×
Siderite	9.8	2.51×10^{-9}	95.3	1.74 ×
Witherite	9.8	2.51×10^{-9}	95.3	1.74 ×
Rhodochrosite	9.8	2.51×10^{-9}	95.3	1.74 ×
Strontianite	9.8	2.51×10^{-9}	95.3	1.74 ×
Dawsonite	9.8	1×10^{-7}	62.8	

Appendix

B. Supplementary data

Download Word document (5MB)Help with docx files

Additional data and model results.

References

Appelo and Postma, 1994

C.J.A. Appelo, D. Postma**Geochemistry, Groundwater and Pollution**

A.A. Balkema, Rotterdam, Netherlands (1994)

Appelo et al., 2002

C.A.J. Appelo, M.J.J. Van Der Weiden, C. Tournassat, L.Charlet**Surface complexation of ferrous iron and carbonate on ferrihydrite and the mobilization of arsenic**

Environ. Sci. Technol., 36 (14) (2002), pp. 3096-3103

CrossRefView Record in Scopus

Apps et al., 2010

J.A. Apps, L. Zheng, Y. Zhang, T. Xu, J.T. Birkholzer**Evaluation of groundwater quality changes in response to CO_2leakage from deep geological storage**

Transp. Porous Media, 82 (1) (2010), pp. 215-246

CrossRefView Record in Scopus

Bacon et al., 2016

D.H. Bacon, N.P. Qafoku, Z. Dai, E.H. Keating, C.F. Brown**Modeling the impact of carbon dioxide leakage into an unconfined, oxidizing carbonate aquifer**

Int. J. Greenhouse Gas Control, 44 (2016), pp. 290-299

ArticleDownload PDFView Record in Scopus

Cahill and Jakobsen, 2013

A.G. Cahill, R. Jakobsen**Hydro-geochemical impact of CO_2 leakage from geological storage on shallow potable aquifers: a field scale pilot experiment**

Int. J. Greenhouse Gas Control., 0 (2013)

Cahill et al., 2014

A.G. Cahill, P. Marker, R. Jakobsen**Hydrogeochemical and mineralogical effects of sustained CO_2contamination in a shallow sandy aquifer: a field-scale controlled release experiment**

Water Resour. Res., 50 (2) (2014), pp. 1735-1755

CrossRefView Record in Scopus

Carroll et al., 2009

S. Carroll, Y. Hao, R. Aines**Geochemical detection of carbon dioxide in dilute aquifers**

Geochem. Trans., 10 (4) (2009), pp. 1-18

CrossRefView Record in Scopus

Dafflon et al., 2013

B. Dafflon, Y. Wu, S.S. Hubbard, J.T. Birkholzer, T.M. Daley, J.D. Pugh, J.E. Peterson, R.C. Trautz**Monitoring CO_2 intrusion and associated geochemical transformations in a shallow groundwater system using complex electrical methods**

Environ. Sci. Technol., 47 (1) (2013), pp. 314-321

CrossRefView Record in Scopus

Dzombak and Morel, 1990

D.A. Dzombak, F.M.M. Morel**Surface Complexation Modeling-Hydrous Ferric Oxide**

John Wiley & Sons, New York (1990)

Harvey et al., 2012

O.R. Harvey, N.P. Qafoku, K.J. Cantrell, G. Lee, J. E.Amonette, C.F. Brown**Geochemical implications of gas leakage associated with geologic CO_2 storage, a qualitative review**
Environ. Sci. Technol., 2013 (47) (2012), pp. 23-36
CrossRefView Record in Scopus

Hou et al., 2014

Z. Hou, D.H. Bacon, D.W. Engel, G. Lin, Y. Fang, H. Ren, Z.Fang**Uncertainty analyses of CO_2 plume expansion subsequent to wellbore CO_2 leakage into aquifers**
Int. J. Greenhouse Gas Control, 27 (2014), pp. 69-80
ArticleDownload PDFView Record in Scopus

Humez et al., 2011

P. Humez, P. Audigane, J. Lions, C. Chiaberge, G. Bellenfant**Modeling of CO_2 leakage up through an abandoned well from deep saline aquifer to shallow fresh groundwater**
Transp. Porous Media, 90 (1) (2011), pp. 153-181
CrossRefView Record in Scopus

Humez et al., 2013

P. Humez, V. Lagneau, J. Lions, P. Negrel**Assessing the potential consequences of CO2 leakage to freshwater resources: A batch-reaction experiment towards an isotopic tracing tool**
Appl. Geochem., 30 (2013), pp. 178-190
ArticleDownload PDFView Record in Scopus

Johnson et al., 1998

J.W. Johnson, K.G. Knauss, W.E. Glassley, L.D. DeLoach, T. A.F.B**Reactive transport modeling of plug-flow reactor experiments: quartz and tuff dissolution at 240 °C**
J. Hydrol., 209 (1–4) (1998), pp. 81-111
ArticleDownload PDFView Record in Scopus

Jordan et al., 2007

N. Jordan, N. Marmier, C. Lomenech, E. Giffaut, J.-J.Ehrhardt**Sorption of silicates on goethite, hematite, and magnetite: experiments and modelling**
J. Colloid Interface Sci., 312 (2) (2007), pp. 224-229
ArticleDownload PDFView Record in Scopus

Y.K. Kharaka, D.R. Cole, S.D. Hovorka, W.D. Gunter, K.G. Knauss, B.M. Freifeld**Gas-water-rock interaction in Frio Fromation following CO_2 injection: implications for the storage of greenhouse gases in sedimentary basins**
Geology, 34 (2006), pp. 577-580
CrossRefView Record in Scopus

Y.K. Kharaka, J.J. Thordsen, S.D. Hovorka, H.S. Nance, D. R. Cole, T.J. Phelps, K.G. Knauss**Potential environmental issues of CO_2 storage in deep saline aquifers: geochemical results from the Frio-I Brine Pilot test, Texas, USA**
Appl. Geochem., 24 (2009), pp. 1106-1112
ArticleDownload PDFView Record in Scopus

Y.K. Kharaka, J.J. Thordsen, E. Kakouros, G. Ambats, W.N.Herkelrath, J.T. Birkholzer, J.A. Apps, N.F. Spycher, L. Zheng, R.C.Trautz, H.W. Rauch, K. Gullickson**Changes in the chemistry of shallow groundwater related to the 2008 injection of CO_2 at the ZERT Field Site, Bozeman, Montana**
Environ. Earth Sci., 60 (2) (2010), pp. 273-284
CrossRefView Record in Scopus

F.E. Kirk**Variation in energy available to populations of subsurface anaerobes in response to geological carbon storage**
Environ. Sci. Technol., 45 (2011), pp. 6676-6682
CrossRefView Record in Scopus

M.F. Kirk, E.F. Santillan, R.E. Sanford, S.J. Altman**CO_2-induced shift in microbial activity affects carbon trapping and water quality in anoxic bioreactors**
Geochim. Cosmochim. Acta, 122 (2013), pp. 198-208
ArticleDownload PDFView Record in Scopus

K. Kirsch, A.K. Navarre-Sitchler, A. Wunsch, J.E. McCray**Metal release from sandstones under experimentally and numerically simulated CO_2 leakage conditions**
Environ. Sci. Technol., 48 (2014), pp. 1436-1442
CrossRefView Record in Scopus

Lasaga et al., 1994

A.C. Lasaga, J.M. Soler, J. Ganor, T.E. Burch, K.L. Nagy**Chemical weathering rate laws and global geochemical cycles**
Geochim. Cosmochim. Acta, 58 (1994), pp. 2361-2368
View Record in Scopus

Lawter et al., 2016

A. Lawter, N.P. Qafoku, G. Wang, H. Shao, C.F. Brown**Evaluating impacts of CO_2 intrusion into an unconsolidated aquifer: I. Experimental data**
Int. J. Greenhouse Gas Control, 44 (2016), pp. 323-333
ArticleDownload PDFView Record in Scopus

Lemieux, 2011

J.-M. Lemieux**Review: the potential impact of underground geological storage of carbon dioxide in deep saline aquifers on shallow groundwater resources**
Hydrogeol. J., 19 (4) (2011), pp. 757-778
CrossRefView Record in Scopus

Little and Jackson, 2010

M.G. Little, R.B. Jackson**Potential impacts of leakage from deep CO_2 geosequestration on overlying freshwater aquifers**
Environ. Sci. Technol., 44 (23) (2010), pp. 9225-9232
CrossRefView Record in Scopus

Lu et al., 2010

J.M. Lu, J.W. Partin, S.D. Hovorka, C. Wong**Potential risks to freshwater resources as a result of leakage from CO_2 geological storage: a batch-reaction experiment**
Environ. Earth Sci., 60 (2) (2010), pp. 335-348
CrossRefView Record in Scopus

McGrath et al., 2007

A.E. McGrath, G.L. Upson, M.D. Caldwell**Evaluation and mitigation of landfill gas impacts on cadmium leaching from native soils**
Ground Water Monit. Remidiat., 27 (4) (2007), pp. 99-109
CrossRefView Record in Scopus

Millington and Quirk, 1961

R.J. Millington, J.P. Quirk**Permeability of porous solids**
Trans. Faraday Soc., 57 (0) (1961), pp. 1200-1207
CrossRefView Record in Scopus

Numerical Dynamics**Multibase MS Excel add-in developed by Numerical Dynamics, Inc., 2-3-1 Marunouchi Chiyoda Tokyo Japan**
NumericalDynamics.com (2014)

J. Palandri, Y.K. Kharaka**A compilation of rate parameters of water-mineral interaction kinetics for application to geochemical modeling**
US Geol. Surv. (2004)
(Open File Report 2004-1068)

J.F. Pankow, J.J. Morgan**Dissolution of tetragonal ferrous sulfide (mackinawite) in anoxic aqueous systems. 2. Implications for the cycling of iron, sulfur, and trace metals**
Environ. Sci. Technol., 14 (2) (1980), pp. 183-186
CrossRefView Record in Scopus

A. Peter, H. Lamert, M. Beyer, G. Hornbruch, B. Heinrich, A.Schulz, *et al.***Investigation of the geochemical impact of CO_2 on shallow groundwater: design and implementation of a CO_2 injection test in Northeast Germany**
Environ. Earth Sci., 67 (2) (2012), pp. 335-349
CrossRefView Record in Scopus

L.N. Plummer, D.L. Parkhurst, T.M.L. Wigley**Critical review of the kinetics of calcite dissolution and precipitation**
J. E. (Ed.), Chemical Modeling in Aqueous System, ACS Symposium Series, Ameridan Chemical Society, Washington, DC (1979)

K. Pruess, C. Oldenburg, G. Moridis**TOUGH2 User's Guide, Version 2.0**
Lawrence Berkeley National Laboratory, Berkeley, CA (1999)

R.C. Smyth, S.D. Hovorka, J. Lu, K.D. Romanak, J.W. Partin, C. Wong, *et al.***Assessing risk to fresh water**

resources from long term CO_2 injection-laboratory and field studies
Energy Procedia, 1 (1) (2009), pp. 1957-1964
ArticleDownload PDFView Record in Scopus

SNL, 2007

SNL**Qualification of Thermodynamic Data for Geochemical Modeling of Mineral–Water Interactions in Dilute Systems (data0.ymp.R5), Report ANL-WIS-GS-000003 REV 01**
Sandia National Laboratories, Las Vegas, Nevada (2007)
(ACC: DOC.20070619.0007 (2007))

Spangler et al., 2010

L.H. Spangler, L.M. Dobeck, K.S. Repasky, *et al.* **A shallow subsurface controlled release facility in Bozeman, Montana, USA, for testing near surface CO_2 detection techniques and transport models**
Environ. Earth Sci., 60 (2) (2010), pp. 227-239
CrossRefView Record in Scopus

Trautz et al., 2013

R.C. Trautz, J.D. Pugh, C. Varadharajan, L. Zheng, M. Bianchi, P.S. Nico, N.F. Spycher, D.L. Newell, R.A. Esposito, Y. Wu, B. Dafflon, S.S. Hubbard, J.T. Birkholzer**Effect of dissolved CO_2 on a shallow groundwater system: a controlled release field experiment**
Environ. Sci. Technol., 47 (1) (2013), pp. 298-305
CrossRefView Record in Scopus

Varadharajan et al., 2013

C. Varadharajan, C. Tinnacher, J. Pugh, R.C. Trautz, L.Zheng, N.F. Spycher, J.T. Birkholzer, H. Castillo-Michel, R.A. Esposito, P.S. Nico**A laboratory study of the initial effects of dissolved carbon dioxide (CO_2) on metal release from shallow sediments**
Int. J. Greenhouse Gas Control, 19 (0) (2013), pp. 183-211
ArticleDownload PDFView Record in Scopus

Viswanathan et al., 2012

H. Viswanathan, Z. Dai, C. Lopano, E. Keating, J. A.Hakala, K.G. Scheckel, *et al.* **Developing a robust geochemical and reactive transport model to evaluate possible sources of arsenic at the CO_2 sequestration natural analog site in Chimayo, New Mexico**
Int. J. Greenhouse Gas Control., 10 (0) (2012), pp. 199-214
ArticleDownload PDFView Record in Scopus

S. Wang, P.R. Jaffe**Dissolution of a mineral phase in potable aquifers due to CO_2 releases from deep formations; effect of dissolution kinetics**
Energy Convers. Manag., 45 (2004), pp. 2833-2848
ArticleDownload PDFView Record in Scopus

Y. Wei, M. Maroto-Valer, M.D. Steven**Environmental consequences of potential leaks of CO_2 in soil**
Energy Procedia, 4 (0) (2011), pp. 3224-3230
ArticleDownload PDFView Record in Scopus

R.T. Wilkin, D.C. Digiulio**Geochemical impacts to groundwater from geologic carbon sequestration: controls on pH and inorganic carbon concentrations from reaction path and kinetic modeling**
Environ. Sci. Technol., 44 (12) (2010), pp. 4821-4827
CrossRefView Record in Scopus

T. Wolery, C. Jove-Colon**Qualification of Thermodynamic Data for Geochemical Modeling of Mineral-Water Interactions in Dilute Systems. ANL-WIS-GS-000003 REV 01**
Sandia National Laboratories, Las Vegas, Nevada (2007)
(ACC: DOC.20070619.0007)

A. Wunsch, A.K. Navarre-Sitchler, J. Moore, J.E. McCray**Metal release from limestones at high partial-pressures of CO_2**
Chem. Geol., 363 (2014), pp. 40-55
ArticleDownload PDFView Record in Scopus

T. Xu, N. Spycher, E. Sonnenthal, G. Zhang, L. Zheng, K. Pruess**TOUGHREACT version 2.0: A simulator for subsurface reactive transport under non-isothermal multiphase flow conditions**
Comput. Geosci., 37 (6) (2011), pp. 763-774
ArticleDownload PDFView Record in Scopus

Yang et al., 2013

C. Yang, P.J. Mickler, R. Reedy, B.R. Scanlon, K. D. Romanak, J.-P. Nicot, S.D. Hovorka, R.H. Trevino, T. Larson**Single-well push–pull test for assessing potential impacts of CO_2leakage on groundwater quality in a shallow Gulf Coast aquifer in Cranfield, Mississippi**
Int. J. Greenhouse Gas Control, 18 (0) (2013), pp. 375-387
ArticleDownload PDFCrossRefView Record in Scopus

Zheng et al., 2012
L. Zheng, J.A. Apps, N. Spycher, J.T. Birkholzer, Y.K. Kharaka, J. Thordsen, *et al.***Geochemical modeling of changes in shallow groundwater chemistry observed during the MSU-ZERT CO_2 injection experiment**
Int. J. Greenhouse Gas Control, 7 (0) (2012), pp. 202-217
ArticleDownload PDFView Record in Scopus

Zheng et al., 2009
L. Zheng, J.A. Apps, Y. Zhang, T. Xu, J.T. Birkholzer**On mobilization of lead and arsenic in groundwater in response to CO_2 leakage from deep geological storage**
Chem. Geol., 268 (3–4) (2009), pp. 281-297
ArticleDownload PDFView Record in Scopus

Zheng et al., 2016
L. Zheng, N.P. Qafoku, A. Lawter, G. Wang, H. Shao, C.F.Brown**Evaluating impacts of CO_2 intrusion into an unconsolidated aquifer: II. Modeling results**
Int. J. Greenhouse Gas Control, 44 (2016), pp. 300-309
ArticleDownload PDFView Record in Scopus

Zheng et al., 2013
L. Zheng, N. Spycher, J. Birkholzer, T. Xu, J. Apps, Y. Kharaka**On modeling the potential impacts of CO_2 sequestration on shallow groundwater: transport of organics and co-injected H_2S by supercritical CO_2 to shallow aquifers**
Int. J. Greenhouse Gas Control, 14 (0) (2013), pp. 113-127
ArticleDownload PDFView Record in Scopus

Zheng et al., 2015
L. Zheng, N. Spycher, C. Varadharajan, R.M. Tinnacher, J. D.Pugh, M. Bianchi, J. Birkholzer, P.S. Nico, R.C. Trautz**On the mobilization of metals by CO_2 leakage into shallow aquifers: exploring release mechanisms by modeling field and laboratory experiments**
Greenhouse Gases Sci. Technol., 5 (2015), pp. 1-16
CrossRefView Record in Scopus

Zhong et al., 2014
L. Zhong, K.J. Cantrell, D.H. Bacon, J. Shewell**Transport of organic contaminants mobilized from coal through sandstone overlying a geological carbon sequestration reservoir**
Int. J. Greenhouse Gas Control, 21 (2014), pp. 158-164
ArticleDownload PDFView Record in Scopus